nature communications

Article

https://doi.org/10.1038/s41467-025-61725-x

Subversion of mRNA degradation pathways by EWSR1::FLI1 represents a therapeutic vulnerability in Ewing sarcoma

Received: 7 May 2024

Accepted: 30 June 2025

Published online: 16 July 2025

Check for updates

Bartimée Galvan[1,2], Loïc Ongena[1], Jonathan Bruyr[1], Gregory Fettweis[1,3], Eva Lucarelli[1], Arnaud Lavergne[4], Emeline Mariavelle[1], Tina M. O'Grady[1,5], Zahrat El Oula Hassoun[1,6], Margaux Claes[1], Laurence Dubois[1], Kevin A. W. Lee[7], Véronique Kruys[8], Cyril Gueydan[8], Jules Durand[9,10], Eric Hervouet[9,10], Florian H. Geyer[11,12,13], Ana Banito[11,14], Roland Imle[11,14,15], Lianghao Mao[11,12,16], Ashok K. Jayavelu[11,12,16], Thomas G. P. Grünewald[11,12,13,17], Florencia Cidre-Aranaz[11,12,13], Jean-Claude Twizere[18] & Franck Dequiedt[1]

Many cancers are defined by gene fusions that frequently encode oncogenic transcription factors (TFs), such as EWSR1::FLI1 in Ewing sarcoma (EwS). Here, we report that independently to its canonical roles in transcription, EWSR1::FLI1 also functions as an mRNA decay factor, reshaping mRNA stability in EwS. This function participates in EWSR1::FLI1 tumorigenicity and involves interactions of EWSR1::FLI1 with the CCR4-NOT deadenylation complex via its EWSR1-derived low-complexity domain and with the RNA-binding protein HuR/ELAVL1 via its FLI1-derived region. Strikingly, we find that EWSR1::FLI1-mediated mRNA decay antagonizes the normal mRNA protective function of HuR and renders EwS cells highly sensitive to HuR inhibition. Our findings uncover a post-transcriptional function of EWSR1::FLI1 and suggest that targeting mRNA stability mechanisms may offer therapeutic opportunities for EwS.

Gene regulation is a fundamental process in eukaryotes, driving the emergence of different cell types that come together to form specialized tissues sustaining a healthy organism. Defects in gene regulatory circuitries can lead to a broad range of diseases and syndromes, including cancers[1]. Systematic analyses of cancer genomes have revealed the recurrence of a high number of driver somatic mutations in genes encoding factors involved in virtually every aspect of gene expression[2,3]. This is especially striking for sarcomas, the malignant tumors of bone and soft tissue, in which mutations are frequently found in genes such as *TP53*, *ATRX*, *RB1 or c-Myc*[4]. About one third of these cancers are defined by chromosomal translocations leading to pathognomonic gene fusions encoding oncogenic transcription factors (TFs)[5]. Oncogenic fusion TFs, arising in an otherwise stable genomic environment and often acting as key drivers of cancer, are ideal drug targets, making fusion-positive sarcomas particularly vulnerable to precision oncology strategies[6]. In practice, therapeutic targeting of these fusions remains an infrangible challenge, in part due to our incomplete understanding of the molecular mechanisms underlying their pathological functions[5,6].

Ewing sarcoma (EwS), the second most common bone tumor in children and young adults, is a prototypical example of sarcomas caused by fusion TFs. Genetically, it is characterized by a chromosomal translocation between a member of the FET (*FUS*, *EWSR1* and *TAF15*) gene family of RNA-binding proteins (RBPs) and a member of the E-Twenty-Six (ETS) family of TFs (i.e., *FLI1*, *ERG*, *FEV*, *ETV1* and *ETV4*)[7]. The most common EwS fusion is EWSR1::FLI1, in which the amino-terminal (N-terminal) prion-like low-complexity domain (LCD) of EWSR1 is fused in-frame to the carboxy-terminal (C-terminal) region of FLI1, including its DNA-binding domain (DBD)[8]. Considered as the primary driver of disease pathogenesis, EWSR1::FLI1 exhibits important

A full list of affiliations appears at the end of the paper. e-mail: fdequiedt@uliege.be

neomorphic gene regulation properties. By combining the phase transition properties and/or polyaromaticity features derived from the EWSR1 LCD to the DNA-binding properties of FLI1, EWSR1::FLI1 activates de novo enhancers at GGAA microsatellites and modifies the local chromatin environment[9–14]. This results in the transcriptional activation of many cellular genes[7], long-intergenic noncoding RNAs (lincRNAs)-related neogenes[15], miRNAs[16] and enhancer RNAs (eRNAs)[17]. In contrast, EWSR1::FLI1 represses transcription when bound at enhancers/promoters defined by canonical non-repetitive GGAA ETS motifs[13,18] According to current knowledge, EWSR1::FLI1 primarily functions as an aberrant TF, profoundly rewiring the 3D chromatin, epigenetic and transcriptional landscapes of the EwS cell[7,19,20]. The expression level of any gene is governed by the steady-state concentration of translatable mRNAs, which is maintained through the opposing yet coordinated processes of transcription and cytoplasmic decay[21,22]. In most cases, cytoplasmic mRNA turnover is initiated through trimming of the 3′ poly(A) tail by the CCR4-NOT complex quickly followed by the recruitment of the mRNA decapping complex to the 5′ end of the mRNA[23]. Structurally, the CCR4-NOT deadenylation complex is a modular, multi-subunit assembly comprising catalytic and regulatory components. Its core module includes two deadenylases, Ccr4 and Caf1 (also known as CNOT6/6 L and CNOT7/8, respectively), supported by CNOT1, which serves as the central platform for assembling the complex[24]. Additional subunits, including CNOT2, CNOT3, and CNOT9, contribute to structural stability and regulatory functions. Tethering of CCR4-NOT to specific decay targets is mediated by RNA-binding proteins (RBPs) or miRNAs, mainly through its NOT (CNOT2-CNOT3) module[24–28]. Regulation of mRNA stability participates in the dynamics of cellular transcriptomes during critical processes, such as cell division, pluripotency and differentiation[29–32]. Curiously, the extent to which mRNA stability contributes to gene expression in cancer cells has remained mostly unaddressed[33,34]. In recent years, several studies have shown that beyond their canonical roles in mRNA synthesis, some developmental master TFs can achieve control of gene expression by directly affecting mRNA decay[35–39]. However, whether oncogenic TFs might also deregulate mRNA stability to shape the cancer cell transcriptome is yet to be determined[40].

Here, we show that beyond its canonical roles in transcription, EWSR1::FLI1 acts as an mRNA decay factor, dictating an aberrant mRNA stability landscape in EwS. This function participates in EWSR1::FLI1 tumorigenicity and relies on its ability to interact with the CCR4-NOT deadenylation complex via its N-terminal LCD and with the RNA-binding protein HuR (also known as ELAVL1) via its FLI1-derived region. We find that EWSR1::FLI1 subverts the normal mRNA protective function of HuR to instead promote mRNA decay. This function renders EwS cells highly vulnerable to HuR inhibition. Our study provides evidence that deregulation of mRNA decay pathways represents an unanticipated oncogenic driving force in EwS and uncovers new therapeutic opportunities for EwS potentially applicable to other fusion TF-driven cancers.

Results

EWSR1::FLI1 dictates an aberrant mRNA stability landscape in EwS

To interrogate a potential role for EWSR1::FLI1 in mRNA decay, we analyzed genome-wide changes in mRNA stability in EwS cells in the presence and absence of EWSR1::FLI1. To this aim, we used shA673-1c, a well-characterized EwS-derived cell line allowing knockdown (KD) of EWSR1::FLI1 using a doxycycline (dox)-inducible shRNA[41,42]. Following transcription blockage with Actinomycin D (ActD), we assessed and compared the evolution of the steady-state levels of individual mRNAs over time by RNA-seq in shA673-1c cells expressing high (EWSR1::FLI1^{high}, i.e., untreated cells) or low (EWSR1::FLI1^{low}, i.e., dox-treated cells) levels of EWSR1::FLI1 (Fig. 1a). EWSR1::FLI1 KD was confirmed by western blotting analysis (Fig. S1a) and principal component analysis (PCA) of RNA-seq libraries showed the expected clustering among experimental replicates (Fig. S1b). Using a first-order decay kinetic model, we estimated half-lives (HLs) of 7170 individual poly(A) RNAs in EWSR1::FLI1^{high} and EWSR1::FLI1^{low} cells. The median mRNA HL was 7.8 h in EWSR1::FLI1^{high} cells and 12.5 h in EWSR1::FLI1^{low} cells, indicating that expression of EWSR1::FLI1 was associated with reduced mRNA stability in shA673-1c cells (Fig. 1b). To further compare HLs in both conditions, we calculated a HL ratio for each mRNA by dividing the HL in EWSR1::FLI1^{high} cells with that in EWSR1::FLI1^{low} cells. We identified 772 individual mRNAs that were significantly destabilized ($\log_2$ HL ratio < 0, p-value < 0.05, two-sided paired Student's t-test) in EWSR1::FLI1-expressing cells, while only 26 were stabilized ($\log_2$ HL ratio > 0, p-value < 0.05, two-sided paired Student's t-test) (Fig. 1c and Source Data). In EWSR1::FLI1^{high} cells, these 772 mRNAs appeared to be shorter-lived compared to mRNAs whose HL was not affected by EWSR1::FLI1 (median HL 5.9 h vs. 8.1 h, respectively) (Fig. S1c). Altogether, these observations suggested that EWSR1::FLI1 may act as a mRNA destabilizing factor in EwS cells. Gene ontology (GO) analysis of the 772 mRNA transcripts destabilized in the presence of high EWSR1::FLI1 levels revealed a significant enrichment in genes involved in transcription (GO:0006367), mRNA splicing (GO:0000398), cell division (GO:0044772, GO:0090266), apoptosis (GO:0006915) and response to DNA damage (GO:0006974) (Fig. 1d), suggesting that EWSR1::FLI1 controls important mRNA regulons via the regulation of mRNA stability. In contrast, no specific GO term was statistically enriched in mRNA transcripts that were stabilized in EWSR1::FLI1^{high} cells.

To cross-validate these observations, a panel (hereafter called the "decay panel") of 10 transcripts (*STC2*, *DNAJB9*, *ATP8B2*, *FZD1*, *RIOK1*, *ATG5*, *AURKB*, *EIF4E*, *CCNK* and *ZEB2*) was selected from the 772 mRNAs that were destabilized by EWSR1::FLI1 (Figs. 1c and S1d). For each of these mRNAs, we measured mRNA decay after ActD treatment by RT-qPCR (ActD/RT-qPCR) in two EwS cell lines (shA673-1c and shSK-E17T) before and after EWSR1::FLI1 KD and calculated the corresponding HL ratio as described above (i.e., HL in EWSR1::FLI1^{high} relative to the HL in EWSR1::FLI1^{low} cells) (Fig. S1e). In agreement with our RNA-seq analysis, these mRNAs were all destabilized following expression of EWSR1::FLI1 in both EwS cell lines (Fig. 1e). Mesenchymal stem cells (MSCs) are the likely cells of origin of EwS and expression of EWSR1::FLI1 in these cells recapitulates many features of EwS cells[43]. To confirm the causal role of EWSR1::FLI1 in the destabilization of mRNA, we assessed the HL of the mRNAs from the decay panel in bone marrow-derived human MSCs (hMSCs) before and after ectopic expression of EWSR1::FLI1. In agreement with the KD experiments in EwS cells, the presence of EWSR1::FLI1 systematically correlated with destabilization of the tested mRNAs in hMSCs, as measured by ActD/RT-qPCR (Fig. 1e). To exclude potential side effects of ActD, we evaluated the stability of the 10 representative mRNAs using Roadblock-qPCR, a 4-thiouridine (4sU)-based approach that measures mRNA stability without transcriptional blockage or pharmacological intervention[44]. This analysis confirmed the destabilization of 7 out of 10 tested transcripts (i.e., *STC2*, *DNAJB9*, *FZD1*, *RIOK1*, *ATG5*, *EIF4E* and *ZEB2*) upon EWSR1::FLI1 expression in shA673-1c cells, further supporting the findings obtained with the ActD approach (Fig. 1e). To further validate these findings genome-wide and across different EwS cell lines, we performed mRNA stability analysis using DiffRAC, a label-free method that leverages changes in exonic and intronic reads to assess differential mRNA stability without pharmacological intervention or RNA labeling[33,45,46]. First, we applied DiffRAC to shA673-1c cells as an orthogonal, unbiased validation of our ActD/RNA-seq pipeline. We observed a significant overlap between transcripts destabilized following EWSR1::FLI1 expression identified by both methods, with 25.5% (166/650) of decay targets detected in both ActD/RNA-seq and DiffRAC datasets (Fig. S1f and Source Data). Building on these

https://doi.org/10.1038/s41467-025-61725-x

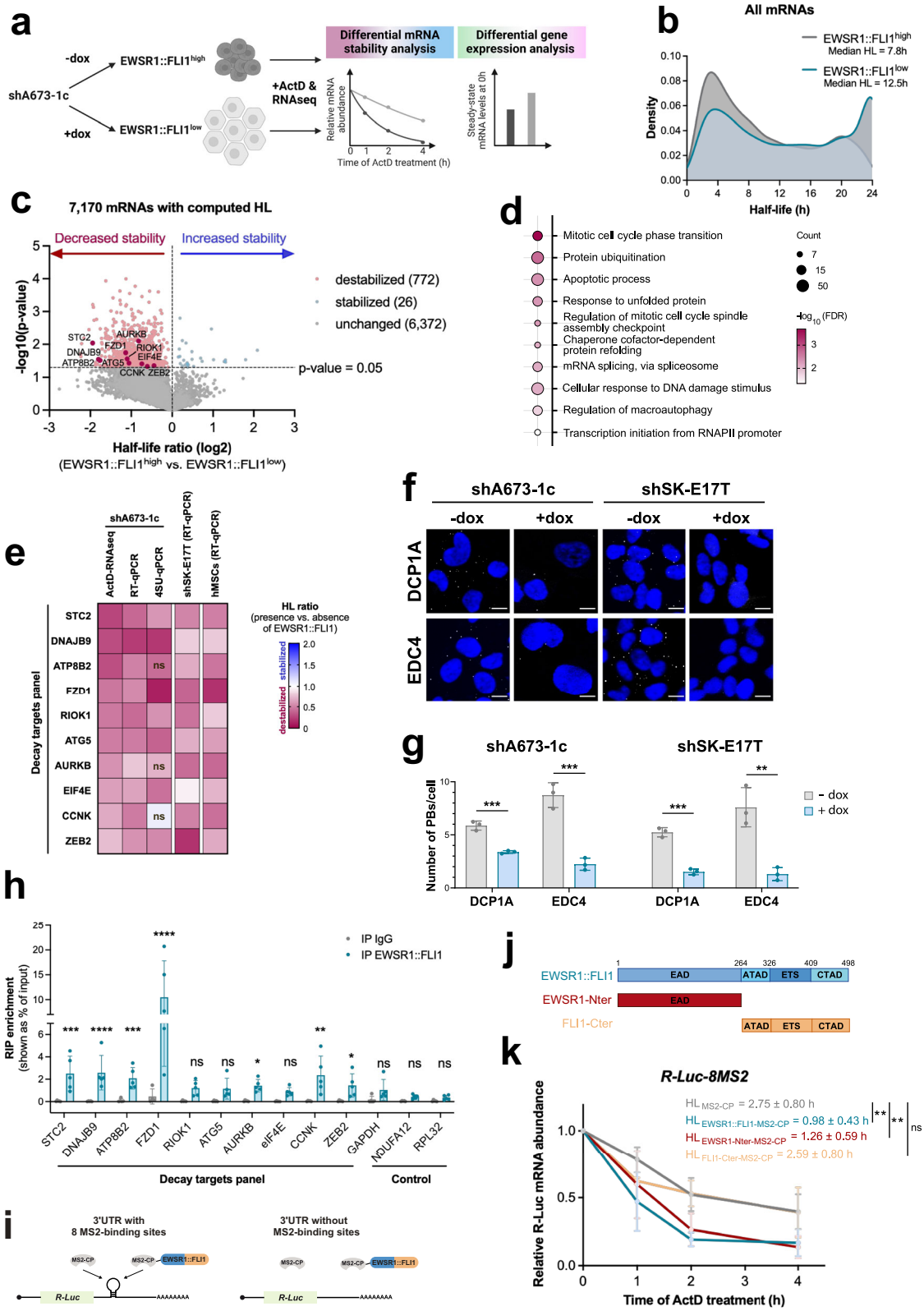

findings, we applied DiffRAC analysis to TC-32 EwS cells knocked down or not for EWSR1::FLI1 using siRNA. In TC-32 cells, DiffRAC identified thousands of transcripts destabilized in the presence of EWSR1::FLI1 ($n = 1998$; FDR-adjusted p-value < 0.05). Notably, almost half of these transcripts ($n = 896$; 44.8%) overlapped with those identified in shA673-1c cells (Fig. S1g and Source Data). Altogether, these results robustly validate our original set of EWSR1::FLI1 decay targets using diverse methods across multiple EwS cell lines and suggest that the destabilization of specific mRNAs might represent an additional molecular function of EWSR1::FLI1.

Processing bodies (P-bodies, or PBs) are microscopic aggregates of mRNA-protein complex (mRNP) that accumulate translationally repressed mRNAs and mRNA-decay associated factors such as decapping protein 1A (DCP1A), enhancer of mRNA decapping 4 (EDC4)

Fig. 1 | EWSR1::FLI1 dictates an aberrant mRNA stability landscape in Ewing sarcoma. a Schematic of the experimental design assessing transcript abundance and stability changes following EWSR1::FLI1 knockdown in shA673-1c cells. Created in BioRender, Galvan, B. (2025) BioRender.com/0001. **b** Half-life (HL) distribution of 7170 transcripts measured by ActD-RNA-seq in EWSR1::FLI1^{high} vs. EWSR1::FLI1^{low} shA673-1c cells. **c** Volcano plot showing significantly destabilized (red) and stabilized (blue) mRNAs in EWSR1::FLI1^{high} vs. EWSR1::FLI1^{low} shA673-1c cells (log2(HL ratio) > 0, *p*-value < 0.05, two-sided paired Student's *t*-test, *n* = 3 independent experiments). Unaffected mRNAs are gray. Horizontal and vertical dotted lines indicate statistical cutoff (*p*-value = 0.05) and log2(HL ratio) = 0, respectively. Transcripts selected for validation are indicated. **d** GO term enrichment of destabilized transcripts from (**c**) (FDR < 0.2, PANTHER analysis; dot size = number of genes; color scale = *p*-value). **e** Heatmap of HL ratios for decay panel transcripts using ActD-RNA-seq, ActD-RT-qPCR or 4SU-qPCR in EWSR1::FLI1^{high} vs. EWSR1::FLI1^{low} shA673-1c cells (first 3 lanes). Validation by ActD-RT-qPCR in shSK-E17T cells and hMSCs shown in last two lanes. Results are means from 3 to 4 independent experiments; *ns* = not significant (one-sample *t*-test). **f** Immunofluorescence of PB markers DCP1A and EDC4 (white) and DAPI (nuclei, blue) in shA673-1c and shSK-E17T cells, -/+dox. Scale = 5 μm. **g** PB quantification from (**f**) as mean ± SD (*n* > 50 cells per replicate over 3 independent experiments). $^{**}p < 0.01$; $^{***}p < 0.001$ (unpaired two-tailed Student's *t*-test). **h** RIP analysis of decay panel and control mRNAs bound to EWSR1::FLI1 in shA673-1c cells (*n* = 5 independent experiments). Data shown as mean % of input ± SD. $^{*}p < 0.05$; $^{**}p < 0.01$; $^{***}p < 0.001$; $^{****}p < 0.0001$ vs. control (unpaired two-tailed Student's *t*-test). **i** Schematic of *R-Luc-8MS2* and *R-Luc-0MS2* reporter mRNAs. **j** Domain structure of EWSR1::FLI1. **k** *R-Luc-8MS2* mRNA stability in HeLa cells co-transfected with MS2-CP-tagged constructs and treated with ActD for 0–4 h (*n* = 5 independent experiments). Mean ± SD $^{**}p < 0.01$; *ns* = not significant compared to MS2-CP (unpaired two-tailed Student's *t*-test). Source data are provided as a Source Data file. Exact *p*-values are provided in the Source Data file.

and subunits of the CCR4-NOT deadenylation complex[47]. Although their precise function is still debated, PBs are closely linked to mRNA metabolism, harboring mRNAs in equilibrium with polysomes or marked for degradation[48]. Changes in PB number can thus serve as a proxy for dysregulated mRNA metabolism. To investigate the impact of EWSR1::FLI1 on PB formation, we analyzed PBs in EWSR1::FLI1^{high} and EWSR1::FLI1^{low} EwS cells, using DCP1A and EDC4 as PB markers. KD of EWSR1::FLI1 was associated with a significant reduction in PB numbers, suggesting that the presence of EWSR1::FLI1 enhances mRNA flux into PBs (Fig. 1f, g). This observation aligns with the idea that EWSR1::FLI1 promotes mRNA decay, although the contribution of other functions of EWSR1::FLI1 to PB metabolism cannot be ruled out[49]. Consistent with its role as a TF, EWSR1::FLI1 predominantly localized in the nucleus of EwS cells but was also observed in the cytoplasm, as discrete foci (Fig. S1h). Co-staining for DCP1A showed that EWSR1::FLI1 cytoplasmic foci are however distinct from PBs (Fig. S1i).

EWSR1::FLI1 largely remodels the transcriptional landscape of EwS cells, modifying the transcription of hundreds of genes contributing to EwS biology[50,51]. One trivial explanation for the effects of EWSR1::FLI1 on mRNA stability could be that it controls the expression of general factors from the mRNA degradation machineries, although this would be difficult to reconcile with our observation that only specific mRNAs, with related functions are destabilized by EWSR1::FLI1. To test this, we first identified genes whose expression levels are controlled by EWSR1::FLI1 by performing a differential gene expression (DGE) analysis in shA673-1c -/+dox (Fig. 1a). We identified 752 and 1,625 mRNAs that were significantly activated and repressed by EWSR1::FLI1, respectively ($|\log_2 FC| > 1$, padj < 0.01, Fig. S1j and Supplementary Data 1). As previously reported, genes activated by EWSR1::FLI1 were strongly enriched for GO terms related to cell division (GO:0051301, GO:0007049), cell proliferation (GO:0008283) and DNA replication (GO:0006260) while repressed genes were enriched for GO terms linked to EMT-related processes, including cell adhesion (GO:0007155), cell migration (GO:0016477) and differentiation (GO:0001649) (Fig. S1k, l)[50]. In contrast, no GO term related to mRNA catabolism [*e.g.*, "regulation of mRNA stability" (GO:0043488), "mRNA catabolic process" (GO:0006402), "CCR4-NOT complex" (GO:0030014), "exosome (RNAse complex)" (GO:0000178), etc.] was significantly associated with down- or upregulated genes. Next, we compared the list of EWSR1::FLI1-regulated genes with a literature-curated list of 66 decay factors (Supplementary Data 2). Out of this list, 61 were detected in our RNA-seq analysis, among which, only 7 exhibited significant changes following EWSR1::FLI1 KD. More specifically, four factors were upregulated (*EXOSC5*, *MPP6*, *ZCCHC3* and *DCP2*) and three factors were repressed (*ZFP36*, *ZFP36L1* and *ZFP36L2*) by EWSR1::FLI1, and all of these are known to promote mRNA decay[52,53] (Fig. S1m). Similarly, we compared the list of EWSR1::FLI1-regulated genes with a list of 371 high-confidence genes encoding PB components collected from the RNP Granule Database[54], 343 of which were detected in our RNA-seq analysis. Out of these, 13 and 16 were respectively up- and down-regulated by EWSR1::FLI1, but none of these genes has been reported to affect PBs biogenesis[54] (Fig. S1n). Together with the finding that only a specific set of functionally related mRNAs are destabilized by EWSR1::FLI1, these observations suggest that mRNA degradation by EWSR1::FLI1 is very unlikely to result from indirect transcriptional changes of decay or PB factors, although we cannot totally exclude this possibility. This conclusion led us to test the possibility that EWSR1::FLI1 might play a direct role in the control of mRNA stability.

EWSR1::FLI1 binds to its decay targets and promotes decay of a tethered reporter mRNA

To this aim, we first assessed whether EWSR1::FLI1-mediated degradation may involve its association with target mRNAs. Using RNA immunoprecipitation (RIP) in EwS cells, we detected EWSR1::FLI1 in association with 7 of the 10 representative mRNAs from the decay panel (i.e., *STC2*, *DNAJB9*, *ATP8B2*, *FZD1*, *AURKB*, *CCNK* and *ZEB2*) (Fig. 1h). In contrast, 3 control mRNAs (*GAPDH*, *NDUFA12* and *RPL32*), whose stability is not affected by the presence of EWSR1::FLI1 were not enriched in the EWSR1::FLI1 immunoprecipitate. These results suggest that EWSR1::FLI1 might associate with specific mRNAs to induce their degradation. To directly test this possibility, we used an mRNA stability tethering assay[35,55]. This assay is based on a *Renilla* luciferase (R-Luc) reporter mRNA carrying eight repeats of the binding sequence for the bacteriophage MS2 coat protein (MS2-CP) in its 3' untranslated region (UTR) (*R-Luc-8MS2*), allowing the specific recruitment of any protein of interest fused to the MS2-CP peptide (Fig. 1i). We found that tethering of EWSR1::FLI1 decreased the stability of the *R-Luc-8MS2* reporter compared to control MS2-CP alone (Fig. 1j, k). Interestingly, destabilization of the reporter was only observed when tethering the N-terminal EWSR1-derived (EWSR1-Nter) region of EWSR1::FLI1. In contrast, the C-terminal FLI1-derived (FLI1-Cter) region, which provides the ETS DNA-binding domain to the fusion had no effect on the reporter stability. Importantly, neither EWSR1::FLI1 nor EWSR1-Nter promoted the degradation of a non-tethered *R-Luc-0MS2* control reporter lacking the MS2-binding sites (Fig. S1o, p). This strongly suggests that the mRNA destabilization of EWSR1::FLI1 is direct and not due to potential indirect effects that might affect mRNA stability globally. Altogether, these observations show that EWSR1::FLI1 can promote mRNA degradation via a mechanism requiring its association with the target mRNA and mediated by its EWSR1-derived LCD.

EWSR1::FLI1 associates with the CCR4-NOT complex via the CNOT2 subunit

In eukaryotic cells, deadenylation is often the first and rate-limiting step of bulk mRNA decay[56,57]. To further investigate a direct role for EWSR1::FLI1 in mRNA degradation, we tested its interaction with CCR4-NOT and PAN2-PAN3, the two major deadenylation

machineries in eukaryotes[58]. Because of its high dynamic range and suitability to high/medium throughput screening, we used a Gaussia luciferase (GLuc) protein complementation assay (gPCA) to screen for protein-protein interactions between EWSR1::FLI1 and the individual subunits of the CCR4-NOT and PAN2-PAN3 complexes (Fig. 2a)[59]. Among all tested interaction pairs, EWSR1::FLI1 only scored positive [normalized luminescence ratio (NLR) > 3.5] with CNOT2, a subunit of the CCR4-NOT complex (Figs. 2b and S2a–c). The interaction with CNOT2 was mapped to the LC N-ter region of EWSR1::FLI1, which is also the region responsible for the mRNA decay activity of the fusion (Figs. 2c and S2d, e). The interaction between EWSR1::FLI1 and CNOT2 was validated by co-immunoprecipitation experiments using FLAG-tagged EWSR1::FLI1 and Myc-tagged CNOT2 and proved to be independent of RNA as it was also observed in the presence of RNAse A (Fig. 2d). We also validated the association between EWSR1::FLI1 and CNOT2 by co-immunoprecipitation of endogenous proteins in EwS cells (Fig. 2e). To map the region of CNOT2 involved in the interaction with EWSR1::FLI1, we undertook co-immunoprecipitation experiments between FLAG-tagged EWSR1::FLI1 and a series of Myc-tagged deletion mutants of CNOT2 (Fig. 2f). These experiments identified the NAR (NOT1 Anchor Region) domain of CNOT2 as the region mediating the interaction with EWSR1::FLI1 (Fig. 2g).

The CCR4-NOT complex consists of two primary modules: a catalytic module, which includes two deadenylases (either CNOT6 or CNOT6L, and either CNOT7 or CNOT8), and the NOT module, composed of CNOT2 and CNOT3. Both the catalytic and NOT modules assemble onto CNOT1, the large scaffolding subunit of the complex (Fig. 2h)[60,61]. Interestingly, endogenous EWSR1::FLI1 copurified with CNOT1 and with CNOT8, one of the deadenylase subunits, indicating an interaction with additional components of the CCR4-NOT complex besides CNOT2 (Fig. 2i, j). To characterize the composition of the EWSR1::FLI1-associated CCR4-NOT complex, we performed coimmunoprecipitations between FLAG-tagged EWSR1::FLI1 and HA-tagged versions of the four catalytic subunits that can be found in CCR4-NOT. While CNOT6L and CNOT8 copurified with EWSR1::FLI1, we detected no association with the CNOT6 or CNOT7 subunits, suggesting that EWSR1::FLI1 specifically associates with the CNOT6L-CNOT8-containing versions of CCR4-NOT (Fig. 2k). Altogether, these results suggest that via its interaction with CNOT2, EWSR1::FLI1 might recruit a fully functional and specific version of the CCR4-NOT deadenylation complex, containing the CNOT6L and CNOT8 deadenylases (Fig. 2l).

The mRNA decay activity of EWSR1::FLI1 relies on its interaction with CNOT2 and supports Ewing sarcomagenesis

Based on our results, we hypothesized that the association with CNOT2 might be critical for the mRNA decay activity of EWSR1::FLI1. In agreement with this, KD of CNOT2 prevented EWSR1::FLI1-mediated degradation of the *R-Luc-8MS2* reporter mRNA, but had no effect on the basal stability of the reporter (i.e., in the absence of EWSR1::FLI1 tethering) (Fig. 3a and Fig. S3a). In addition, knocking down CNOT2 increased the stability of 7 of the 10 representative EWSR1::FLI1 decay targets in EwS cells, namely *ATP8B2*, *RIOK1*, *ATG5*, *AURKB*, *EIF4E*, *CCNK* and *ZEB2*, similarly to knocking down EWSR1::FLI1 (Fig. 3b and Fig. S3b). Notably, 4 of these (*ATP8B2*, *AURKB*, *CCNK* and *ZEB2*) were shown to bind EWSR1::FLI1 in RIP-qPCR experiments (Fig. 1g). Next, we sought to identify a decay-inactive mutant of EWSR1::FLI1, by searching for a mutant in which the interaction with CNOT2 would be compromised. To this aim, we generated a series of deletion mutants of the LC N-ter domain of EWSR1::FLI1 (EWSR1-Nter) (Fig. 3c), as it is the region responsible for the interaction with CNOT2 (Fig. 2c). We found that most of the interaction with CNOT2 was lost upon removal of the first 63 amino acids (aa) of EWSR1-Nter (Fig. 3d and Fig. S3c). Conversely, this 63 aa region alone showed a positive interaction with CNOT2, suggesting that it is not only necessary but sufficient to mediate the interaction between EWSR1::FLI1 and CNOT2. Interestingly, the CNOT2 interacting region is predicted to be less disordered than the rest of the EWSR1-derived intrinsically disordered region (IDR) of EWSR1::FLI1 (Fig. S3d).

When tested in the mRNA degradation reporter assay, EWSR1-Nter lacking the 63 aa CNOT2-interacting region (Δ63EWSR1-Nter) was unable to promote degradation of the *R-Luc-8MS2* reporter (Fig. 3e and Fig. S3e). Furthermore, removal of the CNOT2-interacting region dramatically reduced the ability of EWSR1::FLI1 to promote degradation of its representative decay targets when expressed in hMSCs (Fig. 3f and Fig. S3f). Altogether, these results demonstrate that the degradative activity of EWSR1::FLI1 relies on its ability to interact with CNOT2 via the first 63 aa of its EWSR1-derived domain.

Next, we sought to investigate the importance of EWSR1::FLI1 decay function for its oncogenic properties. To this aim, we designed a KD/rescue system to replace endogenous EWSR1::FLI1 by its decay-defective version (i.e., Δ63EWSR1::FLI1) in A673 EwS cells[62]. As a first step, we engineered a A673-derived cell line expressing a dox-inducible shRNA targeting the 3'UTR region of EWSR1::FLI1 (i.e., A673 shEF3'.11). This system specifically targets endogenous EWSR1::FLI1 while allowing expression of FLAG-tagged full-length EWSR1::FLI1 or Δ63EWSR1::FLI1, as these ectopically expressed versions lack any 3'UTR. Efficient knockdown of endogenous EWSR1::FLI1 and comparable reexpression of FLAG-tagged constructs were assessed by western blotting analysis (Fig. S3g). Taking advantage of our KD/rescue system, we next evaluated the oncogenic potential of Δ63EWSR1::FLI1 using in vitro and in vivo assays. In colony formation assays, we observed that A673 cells rescued with the decay-defective Δ63EWSR1::FLI1 formed significantly less colonies than those rescued with full-length EWSR1::FLI1 (Fig. 3g). Accordingly, xenograft experiments showed significantly (p-value = 0.0014) reduced tumor growth in mice injected with EwS cells expressing the Δ63EWSR1::FLI1 mutant, compared to those expressing full-length EWSR1::FLI1 (Fig. 3h). Together, these data indicate that the mRNA degradative activity of EWSR1::FLI1 contributes to its oncogenic properties.

The transcriptional, splicing and decay activities of EWSR1::FLI1 are uncoupled

Our results showed that the EWSR1-derived region of EWSR1::FLI1 is essential for its mRNA decay activity. This region, which is also involved in EWSR1::FLI1 transcriptional function is a LC IDR containing 30 degenerate hexapeptides repeats (DHRs) with a conserved tyrosine residue (consensus SYGQQS) (Fig. 4a). Replacing the tyrosine residues within the first 17 DHRs by aliphatic amino acids such as alanine (A) or isoleucine (I) completely abrogates the potent transactivating activity of the EWSR1-derived region and transformation in NIH3T3 cells[63]. By contrast, replacing the tyrosines by an aromatic residue, such as phenylalanine (F), has no effect, indicating that aromaticity of the tyrosine residue within these 17 SYGQQS repeats is critical for the oncogenic transcriptional properties of EWSR1::FLI1[63]. To investigate whether these features might also be important for the mRNA decay activity of EWSR1::FLI1, we first tested the interactions between CNOT2 and three different tyrosine mutants of the EWSR1::FLI1 N-ter region: a Y-to-I (SIGQQS), a Y-to-A (SAGQQS) and a Y-to-F (SFGQQS) mutant[63] (Fig. 4a). We found that the SIGQQS and SAGQQS mutants were unable to interact with CNOT2, whereas the SFGQQS mutant retained strong association (Fig. 4b). Interestingly, structural disorder prediction integrating multiple prediction tools along the sequences of these three tyrosine mutants consistently showed that the local higher-order state observed within the first 63 aa was lost when tyrosines are replaced with alanines or isoleucines but not phenylalanines (Fig. S4a). This

https://doi.org/10.1038/s41467-025-61725-x

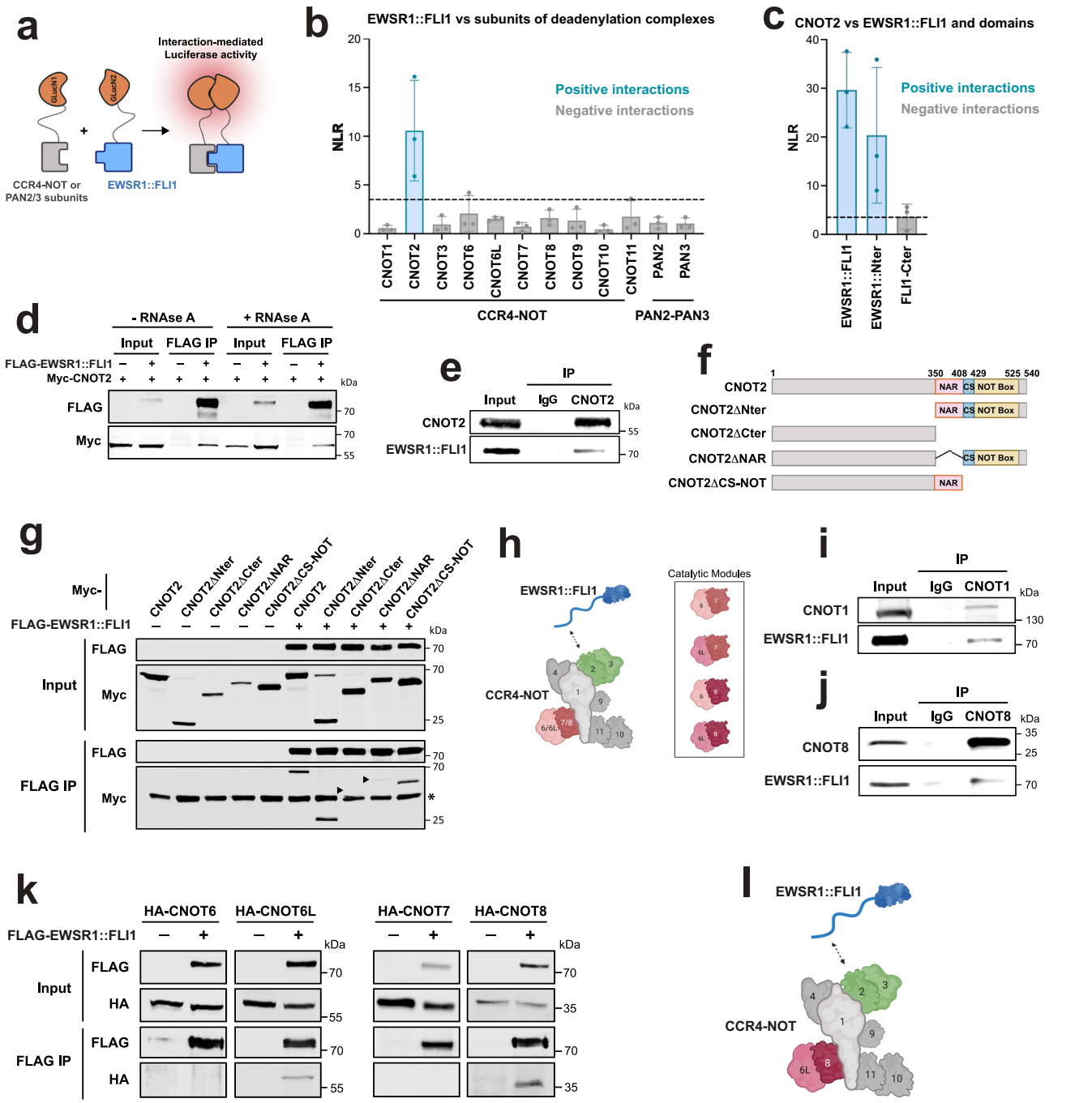

Fig. 2 | EWSR1::FLI1 interacts with the CCR4-NOT deadenylation complex. **a** Schematic of the Gaussia luciferase protein complementation assay (gPCA). GLucN1 and GLucN2 are inactive fragments of Gaussia luciferase. See Cassonnet et al. [59] for more details. Created in BioRender. Galvan, B. (2025) BioRender.com/0002. **b** gPCA normalized luminescence ratios (NLR) of interactions between EWSR1::FLI1 and individual subunits of CCR4-NOT and PAN2-PAN3 complexes. Deadenylase subunits were fused to GLucN1; EWSR1::FLI1 to GLucN2. Blue bars denote interacting pairs (NLR > threshold of 3.5, dotted line); gray bars indicate non-interacting pairs. Data represent means ± SD ($n = 3$ independent experiments). **c** gPCA NLR values for interactions between CNOT2 and full-length EWSR1::FLI1, EWSR1-Nter and FLI1-Cter. EWSR1::FLI1 constructs are fused to GLucN1 (EWSR1::FLI1) or to GLucN2 (CNOT2). Data are means ± SD ($n = 3$ independent experiments). **d** Co-immunoprecipitation (IP) of FLAG-EWSR1::FLI1 with Myc-CNOT2 from HEK293T lysates ± RNAse A treatment. Input lysates and IPs were probed by anti-FLAG and anti-Myc immunoblotting. **e** Co-IP between endogenous CNOT2 and EWSR1::FLI1 in shA673-1c cells. **f** Domain architecture of CNOT2 deletion constructs. FL full-length, NAR NOT1 anchor region, CS connecting sequence. Created in BioRender. Galvan, B. (2025) BioRender.com/0003. **g** Co-IP of FLAG-EWSR1::FLI1 with Myc-tagged CNOT2 truncation mutants in HEK293T cells. Arrows denote expected bands; asterisk indicates non-specific signal. **h** Structure model of the CCR4-NOT complex. NOT module subunits (green), catalytic module subunits (red), CNOT1 scaffold (light grey), and accessory subunits (dark grey) are indicated. Alternate catalytic module configurations are shown (right box). Created in BioRender. Galvan, B. (2025) BioRender.com/0004. **i**, **j** Co-IP between endogenous CNOT1 (**i**) or CNOT8 (**j**) and EWSR1::FLI1 in shA673-1c cells. **k** Co-IP of FLAG-EWSR1::FLI1 with HA-tagged CCR4-NOT subunits in HEK293T cells. **l** Schematic of the EWSR1::FLI1-associated CCR4-NOT module. Created in BioRender. Galvan, B. (2025) BioRender.com/0005. All IPs in Fig. 2 were replicated ≥ 2 times. Source data are provided as a Source Data file.

https://doi.org/10.1038/s41467-025-61725-x

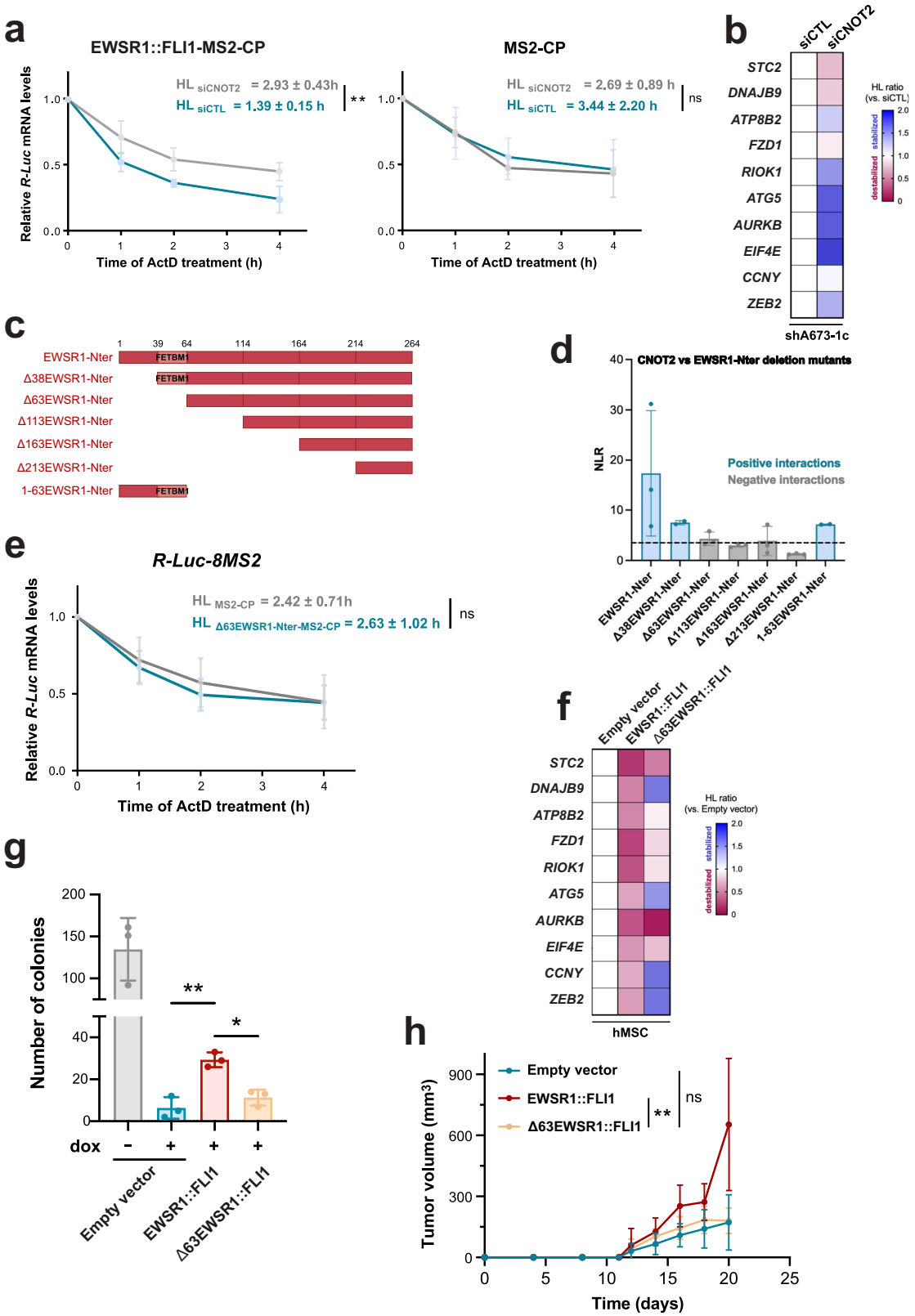

observation is consistent with previous studies showing that order propensity of the EWSR1 LCD is decreased by mutating tyrosines into alanines or isoleucines but not phenylalanines[63,64]. Importantly, the SIGQQS mutant, which has lost its ability to associate with CNOT2 was also unable to destabilize the *R-Luc-8MS2* reporter mRNA in the tethering assay (Fig. 4c). These observations show that both the transcriptional and mRNA decay functions of EWSR1::FLI1 rely on similar features of its LC region, i.e., the presence of a high number of aromatic residues within a highly disordered structure.

These findings prompted us to investigate whether the transcriptional and decay activities of EWSR1::FLI1 might be functionally linked. To address this issue, we first tested whether EWSR1::FLI1 decay targets are transcribed from genes that are transcriptionally regulated

Fig. 3 | EWSR1::FLI1 mRNA decay activity depends on CNOT2 and supports Ewing sarcomagenesis. a mRNA stability of the *R-Luc-8MS2* mRNA reporter in HeLa cells transfected with control (*siCTL*, blue) or CNOT2-targeting (*siCNOT2*, grey) siRNA, and expressing either EWSR1::FLI1-MS2-CP (left) or MS2-CP (right). Data are means ± SD ($n = 4$ independent experiments). $^{**}p < 0.01$; *ns* = not significant (Student's *t*-test, two-tailed, unpaired). HL half-life. **b** Heatmap showing HL ratios for decay panel mRNAs in shA673-1c cells following CNOT2 knockdown. HL ratio = HL (*siCTL*) / HL (*siCNOT2*). Data are means from 3-5 independent experiments. **c** Schematic of EWSR1-Nter-deletion mutants. FETBM1: FET binding module (as described in Linden et al.[134]). **d** gPCA NLR values for interactions between CNOT2 and EWSR1-Nter mutants. Constructs are fused to GLucN1 (EWSR1-Nter deletion mutants) or GLucN2 (CNOT2). Data are means ± SD ($n = 3$ independent experiments; $n = 2$ for Δ63EWSR1-Nter). Positive (> NLR cut-off of 3.5, dotted line) and negative interactions are in blue and gray, respectively. **e** *R-Luc-8MS2* reporter stability in HeLa cells co-transfected with Δ63EWSR1-Nter-MS2-CP (blue) or MS2-CP control (grey). Data are means ± SD ($n = 5$ independent experiments). *ns* = not significant (Student's *t*-test, two-tailed, unpaired). **f** Heatmap showing HL ratios of decay panel mRNAs upon expression of FLAG-tagged EWSR1::FLI1 or Δ63EWSR1::FLI1, or control FLAG empty vector (CTL) in hMSCs. HL ratio = HL (EWSR1::FLI1 construct) / HL (CTL). Data are means ($n \geq 2$ independent experiments). **g** Quantifications of soft agar colony formation in A673 shEF3'.11 cells after endogenous EWSR1::FLI1 knockdown (+ dox) and rescue with FLAG empty vector (blue), FLAG-EWSR1::FLI1 (red), or FLAG-Δ63EWSR1::FLI1 (yellow). Control: cells rescued with the empty vector before knockdown (-dox, gray). Data are means ± SD ($n = 3$ independent experiments). $^{**}p < 0.01$, $^{*}p < 0.05$, ns = not significant (Student's *t*-test, two-tailed, paired). **h** Tumor volumes from A673 shEF3'.11 xenografts following endogenous EWSR1::FLI1 knockdown (+ dox) and rescue with FLAG empty vector (blue), FLAG-EWSR1::FLI1 (red), or FLAG-Δ63EWSR1::FLI1 (yellow). Data are means ± SEM from 8 mice (Empty vector, Δ63EWSR1::FLI1) or 7 mice (EWSR1::FLI1). $P = 0.0014$ (Mann-Whitney test, one-tailed); *ns* = not significant. Source data are provided as a Source Data file. Exact *p*-values are provided in the Source Data file.

by EWSR1::FLI1. To define the transcriptional target genes of EWSR1::FLI1, we used three different approaches: we considered genes that (i) were modulated after EWSR1::FLI1 KD in our DGE analysis (Supplementary Data 1), or (ii) were bound by EWSR1::FLI1 as determined by ChIP-seq[13,65] or (iii) were both modulated following EWSR1::FLI1 KD and bound by EWSR1::FLI1 (Fig. 4d). For genes that were deregulated following KD of EWSR1::FLI1, we also distinguished between genes that were down- and up-regulated by EWSR1::FLI1 (Fig. S4b and Source Data). We also sub-categorized EWSR1::FLI1-bound genes depending on ChIP peak location and considered genes harboring at least a peak either at the promoter (i.e., within 2 kb upstream of the transcription start site) or within the gene body (Fig. S4c and Source Data). None of these datasets showed a significant overlap with EWSR1::FLI1 mRNA decay targets, suggesting that the mRNA decay targets of EWSR1::FLI1 are not transcribed from genes that are regulated nor bound by EWSR1::FLI1. Although EWSR1::FLI1 controls largely different sets of mRNAs via its transcriptional and decay activities, it is still possible that EWSR1::FLI1 achieves control over the same biological functions through coordinated action of both activities on distinct sets of genes. To test this, we compared the GO terms enriched in EWSR1::FLI1-modulated genes (either downregulated or upregulated after KD) with those enriched in EWSR1::FLI1 mRNA decay targets. Interestingly, we found that GO terms related to mitotic cell cycle (GO:0022402, GO:0007346, GO:0044772, GO:0000082, GO:1901976, GO:1903504, GO:0033047), gene expression (GO:0045893) and response to stress (GO:0033554) were enriched in both the genes that are activated by EWSR1::FLI1 and in EWSR1::FLI1 mRNA decay targets (Fig. S4d). Similarly, we found that GO terms related to RNA processing (GO:0006396, GO:0006397, GO:0008380) and apoptotic processes (GO:0008219, GO:0006915) were enriched in EWSR1::FLI1-repressed genes and EWSR1::FLI1 mRNA decay targets (Fig. S4e). Together, this indicates that although the transcriptional and mRNA decay activities of EWSR1::FLI1 concern different mRNAs, some of these mRNAs might encode functionally related proteins.

To more directly test whether the mRNA decay function of EWSR1::FLI1 might be linked to its transcriptional activity, we used two previously published transcription-defective mutants of EWSR1::FLI1, i.e., a deletion mutant lacking most of the ETS DNA-binding domain (ΔETS-EWSR1::FLI1)[66,67] and a mutant in which all tyrosines in the LCD (i.e., including 30 tyrosines inside DHRs and 7 additional tyrosines outside DHRs) are mutated into serines (YS37EWSR1::FLI1)[68] (Fig. 4e). The Y-to-S mutations abolish the phase transition ability and the DNA-binding and transcriptional activation properties of EWSR1::FLI1[68]. Compared to wild-type EWSR1::FLI1, the YS37EWSR1::FLI1 mutant did not show any association with CNOT2, further confirming the importance of the conserved tyrosines in the LC region of EWSR1::FLI1 for the interaction with CNOT2. In contrast, the ΔETS-EWSR1::FLI1 mutant, which is unable to bind DNA and transcriptionally inactive, retained full association with CNOT2 (Figs. 4f and S4f). This allowed us to test its ability to induce mRNA decay. When expressed in hMSCs, the ΔETS-EWSR1::FLI1 mutant promoted degradation of the representative EWSR1::FLI1 mRNA targets as efficiently as wild-type EWSR1::FLI1 (Fig. 4g and Fig. S4g). These results demonstrate that the ability to bind DNA does not participate in the mRNA decay function of EWSR1::FLI1.

To further disconnect the mRNA decay activity of EWSR1::FLI1 from its transcriptional activity, we examined whether the Δ63EWSR1::FLI1 mRNA decay mutant was still functionally active as a transcription factor. To this aim, we performed a reporter assay using a construct bearing a *Firefly* luciferase (*F-Luc*) gene expressed from a SV40 promoter with 12 GGAA-repeats (Fig. 4h). This reporter is specifically activated by EWSR1::FLI1, because of its unique neomorphic ability to bind GGAA microsatellites[10,62]. Although expressed at lower levels, the Δ63EWSR1::FLI1 mRNA decay mutant behaved as a potent transcriptional activator in this assay and induced levels of F-Luc expression comparable to those induced by full-length EWSR1::FLI1 (Fig. 4h and Fig. S4h). In contrast, the transcriptionally inactive YS37EWSR1::FLI1 mutant[68], the DNA-binding deficient ΔETS-EWSR1::FLI1 mutant or wild-type FLI1, had no effect, as expected. The transcriptional activity of EWSR1::FLI1 has been directly linked to its phase transition properties, which are mediated by its N-ter LCD[68]. To evaluate the effect of deleting the first 63 aa on EWSR1::FLI1 phase transition properties, we performed a previously described biotinylated isoxazole (b-isox) precipitation assay using the Δ63EWSR1::FLI1 mutant[69]. As positive and negative controls respectively, we also included wild-type EWSR1::FLI1 and the YS37EWSR1::FLI1 mutant, the latter lacking phase transition abilities[68]. b-isox-mediated precipitation of Δ63EWSR1::FLI1 was comparable to that of wild-type EWSR1::FLI1, while the YS37EWSR1::FLI1 mutant failed to precipitate, even in the presence of 100 μM of b-isox (Fig. 4i). To confirm these results, we performed a Number and Brightness (N&B) analysis[70,71] and found that EWSR1::FLI1 or the Δ63EWSR1::FLI1 mutant both form aggregates, with comparable stoichiometry of between 3 and 4 molecules (Fig. 4j). These experiments thus show that the transcriptional, phase transition and aggregation properties of EWSR1::FLI1 are not significantly affected in the Δ63EWSR1::FLI1 decay deficient mutant. Taken together, these results indicate that although the transcriptional and decay functions of EWSR1::FLI1 share similar structural and biochemical requirements, they are mechanistically independent.

Besides transcription, EWSR1::FLI1 was recently shown to also play a role in mRNA alternative splicing[72–75]. We thus examined whether the mRNA splicing and decay functions of EWSR1::FLI1 might be coupled. As for transcription, we found no significant overlap between EWSR1::FLI1 splicing[72] and decay mRNA targets (Fig. 4k and Source Data). Of note, we found that GO terms related to RNA processing (GO:0006396, GO:0006397, GO:0008380) and cell death (GO:0008219), which were already significantly over-represented both

https://doi.org/10.1038/s41467-025-61725-x

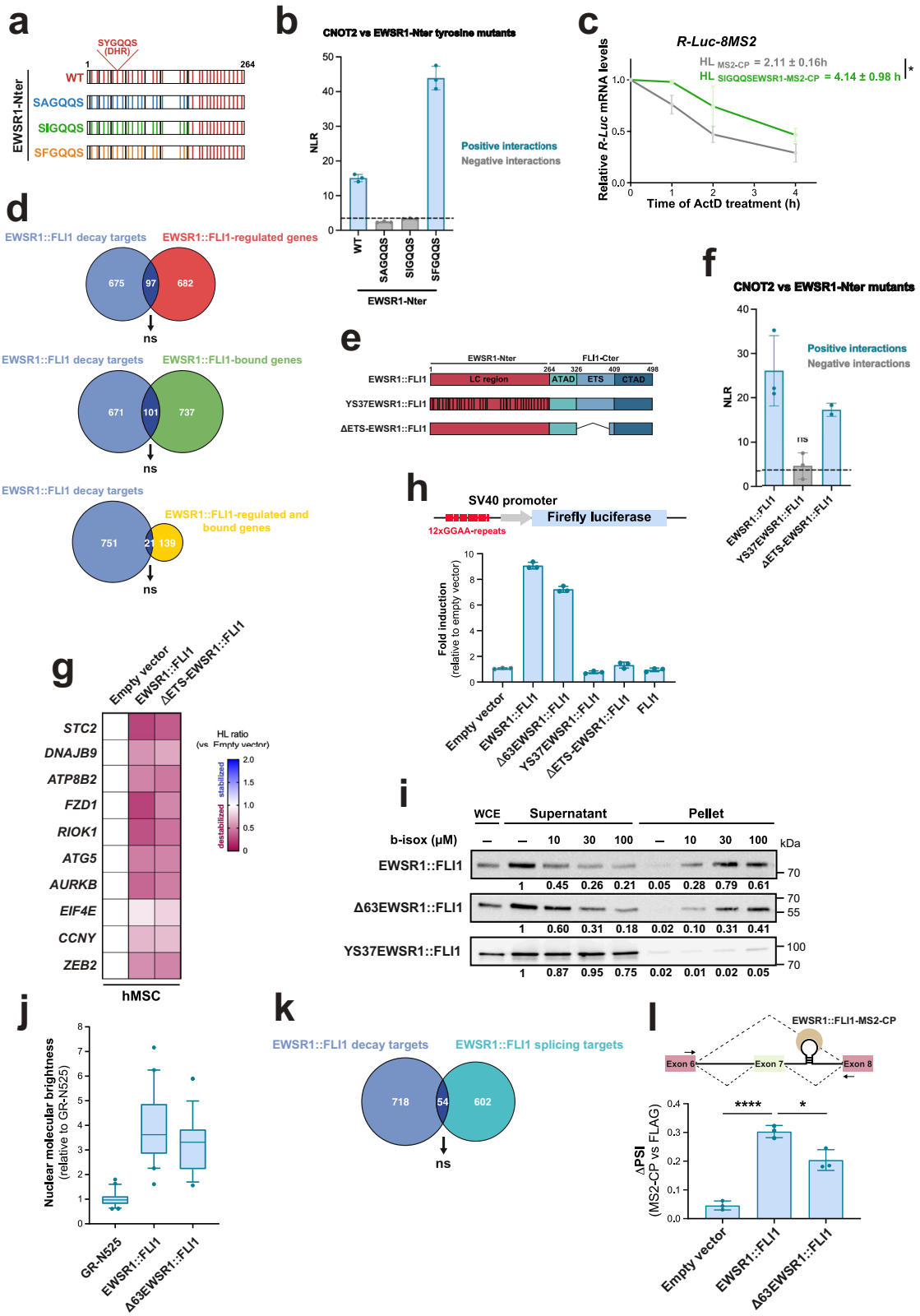

in EWSR1::FLI1 transcriptional and decay targets were also enriched in EWSR1::FLI1 splicing targets (Fig. S4i). This raises the intriguing possibility that EWSR1::FLI1 might control specific biological pathways by the coordination of its transcriptional and post-transcriptional (i.e., mRNA splicing and decay) functions.

Finally, we assessed the integrity of the mRNA splicing function of the Δ63EWSR1::FLI1 decay mutant using a splicing reporter assay (Fig. 4l)[72,76]. In this assay, the Δ63EWSR1::FLI1 mutant behaved similarly to full-length EWSR1::FLI1 and promoted inclusion of a reporter exon, albeit to a slightly smaller extent (Figs. 4l and S4j). Overall, we concluded that the functions of EWSR1::FLI1 in transcription, splicing and decay are molecularly independent and control distinct but functionally related gene repertoires.

Fig. 4 | Transcriptional, splicing and decay activities of EWSR1::FLI1 are uncoupled. a Schematic of EWSR1-Nter tyrosine mutants. Degenerate hexapeptide repeats (DHRs) are indicated by vertical bars. Tyrosines outside DHRs are in black. **b** gPCA NLR values for CNOT2 interactions between EWSR1-Nter and tyrosine mutants. Constructs were fused to GLucN1 (EWSR1-Nter) or GLucN2 (CNOT2). Positive (> NLR cut-off of 3.5, dotted line) and negative interactions are in blue and gray, respectively. Means ± SD ($n = 3$ independent experiments). **c** *R-Luc-8MS2* mRNA stability in HeLa cells expressing SIGQQS-MS2-CP (green) or MS2-CP (grey). Data are means ± SD ($n = 3$ independent experiments). *$p < 0.05$ (Student's *t*-test, unpaired, two-tailed). HL = half-life. **d** Overlaps of decay targets (blue) with EWSR1::FLI1-regulated (red), bound (green) or both (yellow). *ns* = not significant (one-sided Fisher's Exact Test). **e** Schematic of EWSR1::FLI1 and mutants. **f** gPCA NLR for CNOT2 interactions with wild-type or transcription-deficient EWSR1::FLI1 mutants. Constructs are fused to GLucN1 (EWSR1::FLI1) or GLucN2 (CNOT2). Mean ± SD ($n = 3$ independent experiments). **g** Heatmap of decay panel mRNA HL ratios in hMSCs expressing FLAG-tagged EWSR1::FLI1 or ΔETS-EWSR1::FLI1, or control FLAG empty vector (CTL). HL ratio = HL (EWSR1::FLI1 construct) / HL (CTL). ($n \geq 2$ independent experiments). **h** Luciferase transactivation assay using a 12xGGAA F-Luc reporter and R-Luc normalization. Fold induction relative to empty vector. Data are means ± SD ($n = 3$ independent experiments). **i** b-isox precipitation of FLAG-tagged wild-type or mutant EWSR1::FLI1 in HeLa cells. Densitometry normalized to untreated supernatant. WCE whole cell extract. **j** Number and Brightness (N&B) assay in U2OS cells expressing EGFP-tagged constructs. Nuclear molecular brightness (ε) plotted relative to GR-N525. Box plots show medians and 5th-95th percentiles ($n = 2$–4 independent experiments). **k** Overlap between EWSR1::FLI1 decay and splicing targets. *ns* = not significant (Fisher's Exact Test). **l** SMN2 minigene assay in HeLa cells co-transfected with FLAG- or MS2-CP-tagged constructs. Data are means ± SD ($n = 3$ independent experiments). ΔPSI denotes change in exon 7 inclusion relative to control. ****$p < 0.001$; *$p < 0.05$; ns: not significant (one-sample or two-tailed unpaired Student's *t*-test). Source data are provided as a Source Data file. Exact *p*-values are provided in the Source Data file.

EWSR1::FLI1 is recruited to target mRNAs through its interaction with HuR via its CTAD and subverts the normal mRNA protective function of HuR

Our results so far point towards a model in which EWSR1::FLI1 associates with specific mRNAs to promote their degradation via the recruitment of the CCR4-NOT complex. One critical question stemming from this model is how EWSR1::FLI1 might be recruited to its target mRNA transcripts in the absence of any identifiable canonical RNA-binding domain. Because the 3'UTR is a key determinant of mRNA stability[77], we looked whether specific features were associated with the 3'UTR of EWSR1::FLI1 mRNA decay targets. To this aim, we retrieved the 3'UTR sequences of mRNAs that we identified as being destabilized by EWSR1::FLI1 (called hereafter "target 3'UTRs") (Fig. 1b). As a control, we also retrieved the 3'UTR sequences of mRNAs whose stability was unaffected by EWSR1::FLI1 KD (called hereafter "non-target 3'UTRs"). We found that target 3'UTRs were significantly shorter and more AU-rich (i.e., with significantly lower G/C content) than non-target 3'UTRs (Fig. S5a, b). An unbiased heptamer enrichment analysis confirmed the significant enrichment of AU-rich heptamers in target 3'UTRs (Fig. S5c). AU-rich elements (AREs) are important cis-elements for mRNA stability that are recognized by stabilizing or destabilizing ARE-binding proteins (AREBPs)[78]. Based on the above observations, we hypothesized that the stability of EWSR1::FLI1 targets might be controlled by AREBPs. In an unbiased approach, we searched for RBP motifs that might be enriched in target 3'UTRs, compared to non-target. The motifs of two AREBPs, HuR (also known as ELAVL1) and TIA1 were found among the statistically enriched motifs, with HuR standing out as the AREBP with the highest number of enriched motifs and the most statistically enriched motifs (Fig. 5a and Fig. S5d). In agreement with these findings, we found a significant overlap between EWSR1::FLI1 decay targets and the set of HuR-bound mRNAs, as identified by photoactivable ribonucleoside cross-linking and immunoprecipitation (PAR-CLIP)-seq analysis (Fig. 5b and Source Data)[79]. GO analysis of the overlapping mRNAs ($n = 519$) showed a statistical enrichment for GO terms related to cell division (GO:0051301), transcription (GO:0045893) and cell cycle (GO:0007049) (Fig. S5e). Of note, most (359/519; 69.2%) of the overlapping mRNAs between EWSR1::FLI1 decay targets and HuR binding targets had at least one HuR PAR-CLIP peak located in their 3'UTR, with the majority having more than 5 (Fig. S5f). The same held true for the 10 representative EWSR1::FLI1 decay targets, which were all predicted to harbor at least one HuR binding site in their 3'UTR, while 7 of them were predicted to have 5 sites or more (Fig. S5g). However, we did not find any correlation between the number of HuR motifs in a target 3'UTR and its HL ratio in response to EWSR1::FLI1 KD (Fig. S5h). Altogether, these data show that HuR motifs are enriched in the 3'UTR of EWSR1::FLI1 targets, suggesting that EWSR1::FLI1 might be recruited to its decay targets indirectly, via HuR.

In support of this model, co-IP experiments showed that EWSR1::FLI1 copurifies with endogenous HuR in EwS cells (Fig. 5c). In contrast, no association could be detected with the related AREBP TIA1 (Fig. S5i). In a reverse approach, HuR copurified with EWSR1::FLI1 (Fig. 5d), supporting the idea that both proteins can be found within the same complex. PLA experiments confirmed the close interaction between EWSR1::FLI1 and HuR and showed that this interaction was predominantly detected in the cytoplasm (Fig. 5e). Using different deletion mutants of both partners in co-IP experiments, we located the respective interacting interfaces within the FLI1-derived C-ter activation domain (CTAD) of EWSR1::FLI1 (Figs. 5f and 1i) and the RRM3 domain of HuR (Fig. 5g and Fig. S5j). Molecular docking of the 3D structures of the FLI1-derived region of EWSR1::FLI1 and of full-length HuR both confirmed these findings and predicted a stable direct interaction between a sub-region of the EWSR1::FLI1 CTAD and the RRM3 of HuR. The stability of the EWSR1::FLI1/HuR docked complex was further assessed by performing a 500 ns molecular dynamics simulation. The interaction remained stable throughout the simulation and showed that a small region of the unstructured CTAD of EWSR1::FLI1 engages in multiple weak polar interactions with HuR RRM3 (Fig. 5h). Altogether, these results suggest that EWSR1::FLI1 associates with HuR, via its CTAD.

To test the possibility that EWSR1::FLI1 might be recruited to its decay targets via HuR, we used dihydrotanshinone-I (DHTS), a well-characterized chemical interfering with HuR RNA-binding ability[80,81]. We treated EwS cells with DHTS and assessed the stability of the representative EWSR1::FLI1 mRNA decay targets. Similar to knocking down EWSR1::FLI1 or CNOT2, treatment with DHTS led to stabilization of all tested mRNAs (Fig. 5i). More importantly, DHTS significantly reduced the association of EWSR1::FLI1 with most (8 out of 10) of its representative decay targets, supporting the idea that HuR participates in the recruitment of EWSR1::FLI1 onto its target mRNAs (Fig. 5j and Fig. S5k).

Our results show that EWSR1::FLI1 associates with CNOT2 via its LC region and with HuR via a sub-domain of its CTAD. We thus hypothesized that EWSR1::FLI1 might bridge HuR and CNOT2 together, within the same complex. To test this, we performed endogenous co-IP between CNOT2 and HuR in EWSR1::FLI1^{high} and EWSR1::FLI1^{low} shA673-1c cells. HuR co-immunoprecipitated with CNOT2 only in EWSR1::FLI1^{high} cells, thus showing that in the presence of EWSR1::FLI1, HuR acquires the ability to associate with CNOT2 (Fig. 5k). As HuR is a well-described cancer-associated RBP known to inhibit mRNA decay, it was thus unexpected to find it associated with the mRNA destabilization activity of EWSR1::FLI1[79,82]. To clarify this issue, we first investigated the effects of silencing HuR on the stability of the representative EWSR1::FLI1 decay targets. In EWSR1::FLI1^{high} cells, HuR KD strongly increased the HL of all tested EWSR1::FLI1 targets, as would be expected if HuR was responsible for tethering EWSR1::FLI1 onto its

https://doi.org/10.1038/s41467-025-61725-x

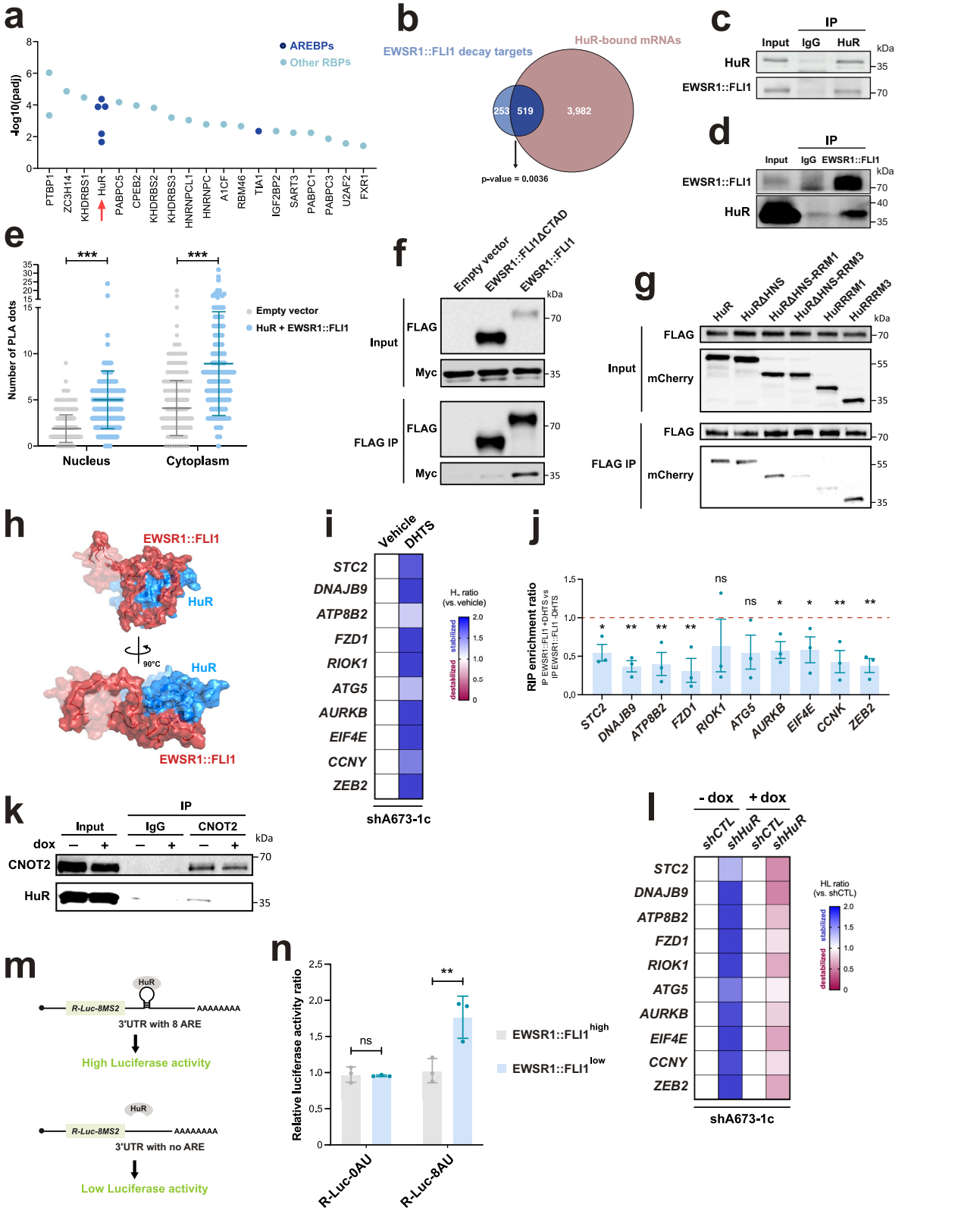

decay targets. Remarkably, HuR KD had the opposite effect in EWSR1::FLI1^{low} EwS cells and decreased the stability of the EWSR1::FLI1 decay targets, in line with the normal mRNA stabilizing function of HuR (Fig. 5l and Fig. S5l). Importantly, we verified that the presence of EWSR1::FLI1 did not interfere with HuR binding to representative EWSR1::FLI1 target mRNAs (i.e., *ATP8B2*, *EIF4E* and *ZEB2*) (Fig. S5m, n). Together, these observations support the model that due to the presence of EWSR1::FLI1, HuR behaves as an mRNA destabilizing factor in EwS cellular context. To strengthen this conclusion, we used a previously described HuR activity reporter assay[55]. This assay is based on a *Renilla* luciferase reporter mRNA carrying eight AREs in its 3'UTR (*R-Luc-8AU*) and allowing the specific recruitment of ectopically expressed HuR. As a negative control, a similar reporter lacking ARE (*R-Luc-0AU*) was used (Fig. 5m). A specific increase in luciferase activity

Fig. 5 | EWSR1::FLI1 co-opts HuR via its CTAD to redirect HuR-associated mRNAs for degradation. a Enrichment of RBP motifs in 3'UTRs of EWSR1::FLI1 decay targets, using non-target 3'UTRs as control. AREBPs (dark blue), non-AREBPs (light blue) and HuR (red arrow) are shown ($p$adj < 0.05). Adjusted P-values (Bonferroni method) were obtained using the MEME-suite. **b** Overlap between EWSR1::FLI1 decay targets and HuR-bound transcripts from (Mukherjee et al.[79]) (one-sided Fisher's Exact Test). **c**, **d** Co-Immunoprecipitation (IP) between endogenous HuR and EWSR1::FLI1 in shA673-1c cells. **e** Quantification of PLA signal in cells co-transfected with Myc-HuR together with a FLAG empty vector (nucleus = 284 cells, cytoplasm = 267 cells) or FLAG-EWSR1::FLI1 (nucleus = 135 cells, cytoplasm = 113 cells). ***$p < 0.001$ (two-way ANOVA). **f**, **g** Co-immunoprecipitation (IP: FLAG) between (**f**) FLAG-tagged EWSR1::FLI1, EWSR1::FLI1ΔCTAD, or the empty FLAG vector and Myc-HuR or (**g**) between FLAG-EWSR1::FLI1 and the indicated mCherry-tagged HuR constructs. **h** Molecular dynamics model of the EWSR1::FLI1/HuR complex. **i** HL ratios of decay panel mRNAs after DHTS vs. DMSO treatments (10 μM, 1h) in shA673-1c cells. HL ratio = HL (DHTS) / HL (DMSO). Data are means ($n = 4$ independent experiments). **j** RIP analysis of decay panel mRNAs bound to EWSR1::FLI1 in shA673-1c cells after DHTS vs. DMSO treatments (10 μM, 1h). RIP enrichment is shown as fold-change relative to *NDUFA12* and *RPL32* control mRNAs. Data are means ± SD ($n = 3$ independent experiments). *$p < 0.05$; **$p < 0.01$; ***$p < 0.001$; ****$p < 0.0001$ (Student's t-test, two-tailed, unpaired). **k** Co-IP between endogenous CNOT2 and HuR in shA673-1c cells ± dox. **l** HL ratios of decay panel mRNAs after HuR knockdown (*shHuR*) vs. control (*shCTL*). HL ratio = HL (*shHuR*) / HL (*shCTL*). Data are means ($n = 3$-4 independent experiments). **m** Schematic of *R-Luc-8AU* and *R-Luc-OAU* reporter mRNAs. **n** HuR-reporter assay using ARE-dependent R-Luc constructs (*R-Luc-8AU* vs. *R-Luc-OAU*) and F-Luc normalization in EWSR1::FLI1^{high} and EWSR1::FLI1^{low} in shA673-1c cells transfected with mCherry-HuR or control vector. Fold induction relative to empty vector (R-Luc/F-Luc ratio normalized to control). Data are means ± SD ($n = 3$ independent experiments). **$p < 0.01$; *ns* = not significant (Student's t-test, two-tailed, unpaired). Source data are provided as a Source Data file. Exact p-values are provided in the Source Data file.

from the *R-Luc-8AU* construct is a proxy for an increase in HuR mRNA stabilizing function. This assay was performed comparatively in EWSR1::FLI1^{high} and EWSR1::FLI1^{low} shA673-1c cells. Consistent with our model, knocking down EWSR1::FLI1 led to a significant increase in R-Luc activity expressed from the *R-Luc-8AU* but not from the *R-Luc-OAU* construct, indicating that the presence of EWSR1::FLI1 inhibits the mRNA stabilizing activity of HuR (Fig. 5n). Altogether, these observations support the model whereby by associating with EWSR1::FLI1 and the CCR4-NOT complex, HuR is turned into an mRNA destabilizing factor in EwS cells.

The decay function of EWSR1::FLI1 unravels a vulnerability of EwS cells towards HuR inhibition

Our findings raised the exciting possibility that EwS cells might be addicted to HuR-mediated EWSR1::FLI1-dependent mRNA degradation. To test this, we first established the effect of DHTS on cell viability in various EwS cell lines (shA673-1c, shSK-E17T and TC71) and non-EwS cell lines (COS-7, MCF-7, MDA-MB-231 and U2OS). Strikingly, we found that EwS cells were consistently more sensitive to DHTS than non-EwS cells (Fig. 6a). To test whether the higher sensitivity of EwS cell lines was due to the presence of EWSR1::FLI1, as predicted by our model or to other features related to the EwS cellular context, we first compared the sensitivity to DHTS of three EwS cell lines (shA673-1c, shSK-E17T and TC71) before and after KD of EWSR1::FLI1. In each case, we found that high levels of EWSR1::FLI1 significantly increased sensitivity towards DHTS (Fig. 6b). Of note, although *HuR* mRNA levels are significantly higher in EwS cells than in non-EwS cancer cells (Fig. S6a), knocking down EWSR1::FLI1 did not affect HuR protein expression, thus ruling out the possibility that changes in sensitivity to DHTS are due to changes in HuR expression levels (Fig. S6b). Compared to EWSR1::FLI1^{low} cells, EwS cell lines expressing high levels of EWSR1::FLI1 were also more sensitive to CMLD-2, another HuR inhibitor (Fig. S6c)[83]. We also compared the sensitivity to DHTS of hMSCs before and after transduction with an EWSR1::FLI1 expression lentivirus. EWSR1::FLI1-expressing hMSCs were dramatically more sensitive to DHTS than non-expressing controls, demonstrating that the sensitivity to HuR inhibition was due to the sole presence of EWSR1::FLI1 and not intrinsic to the mesenchymal precursor cell type from which EwS arise (Fig. 6c). Excitingly, hMSCs expressing the mRNA decay Δ63EWSR1::FLI1 mutant were significantly less sensitive to DHTS than those expressing full-length EWSR1::FLI1, demonstrating that the higher sensitivity of EwS cells to HuR inhibition is linked to the mRNA decay function of EWSR1::FLI1 (Fig. 6d and Fig. S6d). To further evaluate the functional effects of HuR inhibition, we assessed the clonogenic potential of shA673-1c cells in 2D-clonogenic assays. DHTS and CMLD-2 were found to have an IC_{50} of 3 μM (2.91 ± 0.89 μM) and 45 μM (44.68 ± 1.16 μM) respectively, for shA673-1c cells growing in monolayer. Treatment with DHTS or CMLD-2 significantly reduced the clonogenic abilities of shA673-1c cells, even when used at sub-lethal doses (i.e., 2 μM or 35 μM for DHTS or CMLD-2, respectively) (Fig. 6e and Fig. S6e). The inhibitory effect of DHTS was also observed in CFA using two additional EwS cell lines, shSK-E17T ($IC_{50} = 2.37 \pm 0.46$ μM) and MHH-ES1 ($IC_{50} = 8.73 \pm 2.32$ μM (Fig. S6f, g). To more comprehensively evaluate the effects of HuR inhibition, we then used a 3D tumor spheroid model of EwS, which better recapitulates some of the complex processes associated with in vivo tumorigenesis[84]. Multicellular spheroids of shA673-1c cells were treated with various doses of DHTS ranging from 1 μM to 10 μM and spheroid growth was monitored over 4 days. These experiments showed that DHTS inhibited spheroid growth in a dose dependent manner (Fig. 6f, g). Interestingly, even doses of DHTS below IC_{50} (i.e., 2 μM) significantly hindered spheroid growth, indicating that HuR inhibition might interfere with multiple malignant hallmarks of EwS cells (Fig. 6g). In agreement with this idea, we found that DHTS also reduced the migration capacity of shA673-1c cells in 2D assays (Fig. 6h) and their anchorage-independent growth properties, as illustrated by the inability of DHTS-treated cells to form stable 3D spheroids (Fig. 6i). Importantly, we also observed that similarly to DHTS, HuR KD decreased clonogenic proliferation and 3D growth of EwS cells (Fig. 6j, k and Fig. S6h). Finally, we investigated the association between HuR expression and prognosis in a cohort of 166 EwS patients[85–88]. Strikingly, high HuR expression was associated with significantly worse overall survival (p-value = 0.0041), which strongly supports the concept that HuR contributes to EwS pathophysiology (Fig. 6l). High HuR expression levels were also associated with patient status (Dead) and the presence of metastasis at diagnosis (Fig. S6i). Taken together, these results demonstrate that the mRNA decay function of EWSR1::FLI1 contributes to its oncogenic properties in EwS and that its impairment through HuR inhibition represents a promising therapeutic approach for this aggressive cancer.

Discussion

In summary, we have here uncovered a function of EWSR1::FLI1 in mRNA degradation, a process playing a fundamental role in determining the outcome of gene expression. We have characterized the underlying molecular mechanisms, demonstrated its prognostic relevance for patients, and showed that it provides new therapeutic opportunities for patients affected by EwS. Building on recent studies that have reported roles for several master developmental TFs in the control of mRNA stability[35–39], our findings provide evidence that an oncogenic fusion TF can also directly influence mRNA stability to impose a gene expression landscape supporting oncogenic cellular processes. Thus, our findings provide mechanistic insights to the newly emerging idea that deregulation of mRNA stability pathways contribute to cancer development[34,89,90].

The knowledge accumulated during the past three decades has led to a widely-accepted conceptual framework for how EWSR1::FLI1

https://doi.org/10.1038/s41467-025-61725-x

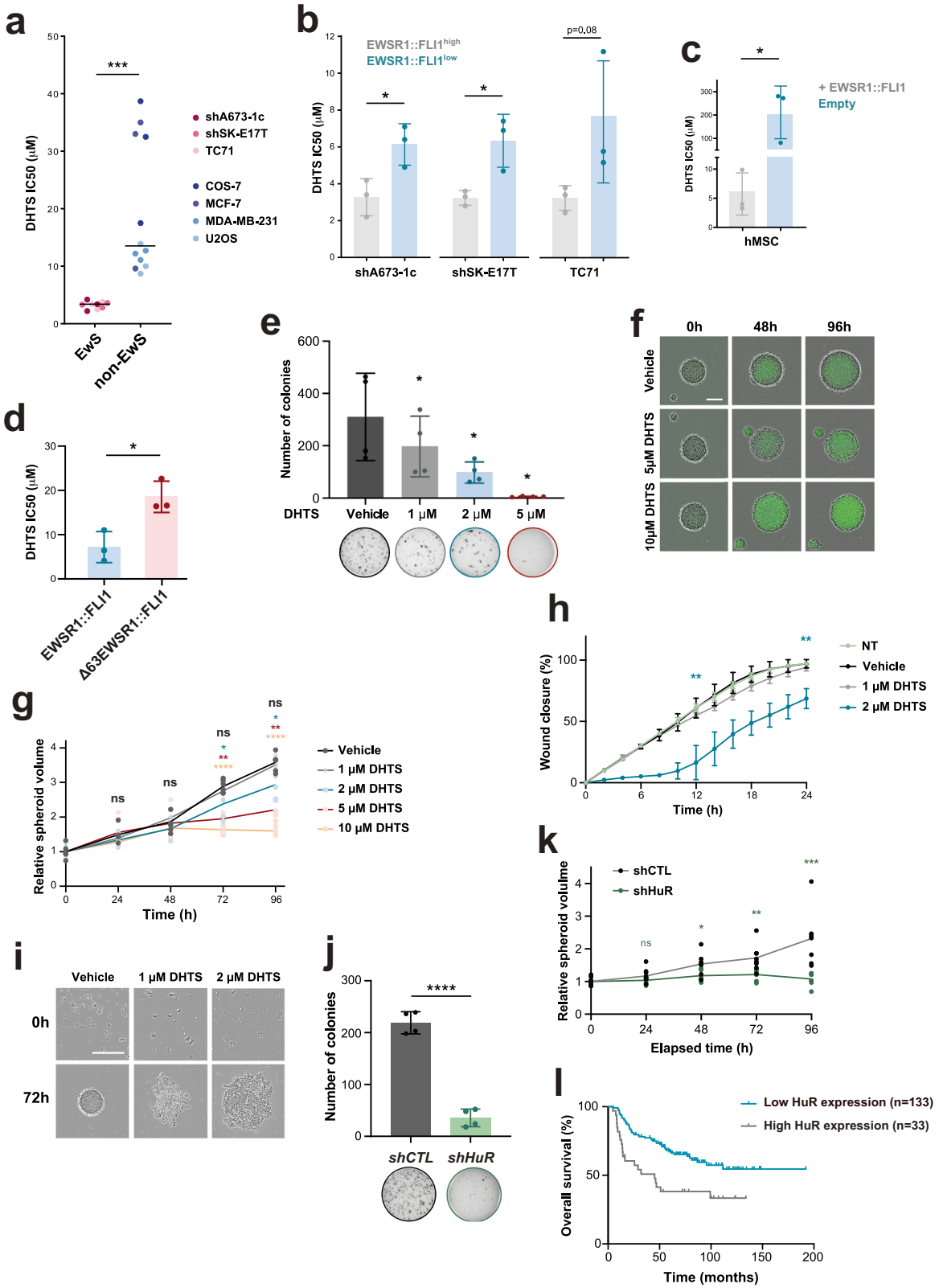

remodels gene expression programs in EwS cells to create a state of strict addiction towards the fusion and drive sarcomagenesis. Specifically, fusion of the LC IDR of EWSR1 to the DBD of FLI1 confers specific neomorphic properties to EWSR1::FLI1 allowing its accumulation at GGAA microsatellites, where it behaves as a pioneer TF, promoting transcription-permissive epigenetic and 3D chromatin landscapes. Our work reveals for the first time that EWSR1::FLI1 also interferes with mRNA stability pathways in EwS cells. Similar to its transcriptional properties, the mRNA decay activity of EWSR1::FLI1 results from the juxtaposition of its LC moiety, mediating interactions with the CCR4-NOT complex, and the FLI1-derived region, which is responsible for the indirect tethering of EWSR1::FLI1 to its target mRNAs via association with HuR. The lack of EWSR1::FLI1 binding in and/or around genes coding for its decay targets together with the observation that a

Fig. 6 | The decay function of EWSR1::FLI1 supports oncogenic transformation in EwS and unravels a vulnerability towards HuR inhibition. a IC_{50} of DHTS in EwS (red) and non-EwS (blue) cell lines. Medians are shown (solid line). $n = 3$ independent experiments. $^{*}p < 0.05$ (Student's *t*-test, unpaired, two-tailed, Welch's correction). **b**, **c** IC_{50} of DHTS in (**b**) EwS cell lines before (EWSR1::FLI1^{high}) and after (EWSR1::FLI1^{low}) EWSR1::FLI1 knockdown and (**c**) hMSCs +/- EWSR1::FLI1 expression. Data are means ± SD ($n = 3$ independent experiments). $^{*}p < 0.05$ (Student's *t*-test, two-tailed, unpaired). **d** IC_{50} of DHTS in hMSCs expressing FLAG-tagged full-length or Δ63EWSR1::FLI1. Data are means ± SD ($n = 3$ independent experiments). $^{*}p < 0.05$ (Student's *t*-test, two-tailed, unpaired). **e** Soft agar colony formation in shA673-1c cells treated with DMSO or DHTS. Data are means ± SD ($n = 4$ independent experiments). $^{*}p < 0.05$ (Student's *t*-test, two-tailed, paired). Representative images are shown. **f** Spheroid assay images at 0, 48 and 96 h after DHTS treatment of shA673-1c cells. Scale = 200 μm. **g** Spheroid volume over time, normalized to $t = 0$ h. ($n = 5$–6 independent replicates). $^{*}p < 0.05$, $^{**}p < 0.01$, $^{****}p < 0.0001$, *ns* = not significant (Student's *t*-test, unpaired, two-tailed). **h** Wound closure assay for shA673-1c cells treated with DHTS, DMSO or untreated (NT). Data are means ± SD ($n = 3$ independent experiments). $^{**}p < 0.01$. (Student's *t*-test, two-tailed, unpaired). **i** Spheroid assay images in shA673-1c cells at 0 and 72 h post-treatment with DHTS or DMSO. Scale = 400 μm. **j** Soft agar colony formation in shA673-1c cells transduced with *shCTL* or *shHuR*. Data are means ± SD ($n = 4$ independent experiments). $^{****}p < 0.0001$ (Student's *t*-test, two-tailed, unpaired). **k** Spheroid volume over time in shA673-1c cells transduced with shCTL or *shHuR*, relative to $t = 0$ h. Data are mean (line) ($n = 4$ independent experiments). $^{*}p < 0.05$, $^{**}p < 0.01$, $^{***}p < 0.001$, *ns* = not significant (Student's *t*-test, two-tailed, unpaired). **l** Kaplan-Meier survival of 166 EwS patients stratified by HuR expression (cut-off: best percentile, log-rank test). Source data are provided as a Source Data file. Exact *p*-values are provided in the Source Data file.

DNA-binding mutant of EWSR1::FLI1 retains mRNA decay activity, suggest a functional disconnection between the abilities of EWSR1::FLI1 to bind to chromatin and to degrade mRNA. This also rules out that EWSR1::FLI1-driven mRNA degradation works within the "imprinting model" framework, whereby promoter/chromatin-associated EWSR1::FLI1 would co-transcriptionally associate with its target mRNAs to later promote their degradation[91]. Interestingly, although the transcriptional and degradation functions of EWSR1::FLI1 appear to control two different mRNA repertoires, we show that both sets contain mRNAs that are functionally linked and are involved in similar biological processes, such as cell cycle and cell proliferation. Together with others, our study thus supports a revisited model for EwS etiology whereby the oncogenic functions of EWSR1::FLI1 lean on the coordinated actions of its transcriptional and post-transcriptional functions, including pre-mRNA splicing and mRNA degradation[72,74,75]. Phase-separation properties are widespread amongst TFs and are thought to be central to transcriptional control[92,93]. The transcriptional functions and neoplastic activity of EWSR1::FLI1 absolutely rely on the liquid-liquid phase transition properties of its LC IDR[20,68,94]. These phase transition abilities are dependent on tyrosine residues within multiple SYGQQS motifs present in the FET-derived LC region. Interestingly, the substitution of these tyrosine residues with serines, which abrogates EWSR1::FLI1 phase transition[68] also abolishes its ability to associate with CNOT2 and mediate mRNA destabilization. These results thus suggest that the ability to engage in phase-separated condensates might also be crucial for EWSR1::FLI1-mediated mRNA decay. This would be consistent with the increasing number of publications recognizing phase transition as the main driving force behind the dynamic assembly and functions of mRNP condensates[69,95]. The observation that the Δ63EWSR1::FLI1 decay mutant still displays phase-separation properties demonstrates that the ability to phase separate is necessary but not sufficient for the mRNA degradative activity of EWSR1::FLI1. While the functional determinants of EWSR1::FLI1 transcriptional activity are spread along the entire EWSR1-derived moiety[63], its mRNA decay activity relies mostly on the N-ter 63 aa of the LCD. Therefore, two features of EWSR1::FLI1 LCD seem crucial for its mRNA degradative activity: (i) the presence of multiple tyrosine residues within the LCD sequence environment of the EWSR1-derived moiety, allowing EWSR1::FLI1 to form phase-separated aggregates and (ii), the first 63 aa, mediating interaction with CNOT2. It was previously described that binding of EWSR1 LCD to transcriptional partners involves polycation-π interactions between tyrosine residues in EWSR1 LCD and basic residues on the partner[14]. Interestingly, the NAR domain of CNOT2 contains several basic residues, thus suggesting that association with CNOT2 might also be mediated by polycation-π interactions. Overall, we suggest a model whereby EWSR1::FLI1 promotes the degradation of specific mRNAs by the capacity of its LCD to form phase-separated condensates, which will favor low-affinity interactions with various factors, including CNOT2 and/or RBPs such as HuR, building up an "EWSR1::FLI1-decaysome". This model does not exclude the possibility that EWSR1::FLI1 associates with CCR4-NOT to also fulfill transcriptional functions. Because of its importance in both the transcriptional and mRNA decay functions of EWSR1::FLI1, the LC region appears as a very attractive therapeutic target for EwS[96]. Unfortunately, intrinsically disordered domains remain exceptionally challenging for current drug strategies that heavily rely upon structural information. Pharmacological targeting of EWSR1::FLI1 has been particularly frustrating so far[97]. Our results might provide viable options for overcoming the challenges of EWSR1::FLI1 druggability. For example, we found that the region encompassing the first 63 aa of EWSR1::FLI1 LCD displays some degree of structural organization that could be exploited to develop specific ligands using the most recent targeted drug discovery approaches[98,99].

The NOT module is essential for the integrity of CCR4-NOT and is thought to act as an interaction surface for RBPs tethering the complex to specific transcripts[24]. It is remarkable that amongst the handful of developmental TFs that have been reported to have roles in mRNA degradation, two (namely, the FLI1-related factor ERG and EBF1) were shown to also recruit CCR4-NOT via the NOT module[35,36]. Specifically, ERG/FLI1 and EWSR1::FLI1 were found to interact with CNOT2, while EBF1 was shown to interact directly with CNOT3. Together with these, our study thus suggests that the NOT module might also serve as a binding platform for TFs and points towards mechanistic similarities between RBP- and TF-mediated mRNA decay. It is important to mention that due to specificities of the gPCA experiment, we cannot rule out the possibility that EWSR1::FLI1 interacts with other subunits of CCR4-NOT. Because EWSR1::FLI1 lacks any canonical RNA-binding domain, we hypothesized that it might be recruited indirectly to its decay targets, via its association with RBPs. In agreement with this, we found that AU-rich motifs for HuR were significantly enriched in the 3'UTR of EWSR1::FLI1 decay targets. In addition, we showed that EWSR1::FLI1 directly interacts with HuR via its CTAD, located in the FLI1-derived moiety, downstream of the ETS DNA-binding domain. Although the role of EWSR1::FLI1 CTAD has been surprisingly overlooked in the past, data indicate that it may be important for the transcriptional regulatory and oncogenic transformation functions of the fusion protein[62,100]. Our findings suggest that the CTAD region can engage in functional interactions with HuR and other RBPs, such as RBFOX2, RBPMS and QKI[35,72]. This region may therefore play a significant role in EWSR1::FLI1's post-transcriptional functions in addition to its transcriptional activities. The mRNA protective activity of HuR is linked to its cytoplasmic localization, which is promoted by cellular stress and is thus favored in cancer cells. Stabilization of various cancer-related transcripts by cytoplasmic HuR is thought to contribute to cancer development and resistance[101]. Because EWSR1::FLI1 promotes cellular stress, it is likely that HuR-mediated mRNA stabilization is highly active in EwS cells[102,103]. Based on our results, we propose a model in which EWSR1::FLI1 precisely controls HuR-mediated mRNA stabilization in EwS cells, by on the one hand promoting cellular stress and on the other hand turning HuR into an mRNA degradation factor.

This mechanism would allow EWSR1::FLI1 to specifically target for degradation transcripts that would otherwise be stabilized by stress-activated HuR. Our study suggests that HuR targeting may offer a therapeutic alternative for EWSR1::FLI1 that would be independent of its LCD[82]. In agreement with this idea, a recent study using a computational predictive pipeline identified HuR as a promising therapeutic target for EwS[104]. DHTS has demonstrated significant anti-cancer potential in preclinical studies, showing efficacy across various cancer types, including hepatocellular carcinoma and colorectal cancer[105]. Currently, DHTS remains in the experimental phase and has not yet been approved for clinical use in humans, as its efficacy and safety profiles are under active investigation. In the context of EwS, validating the therapeutic potential of DHTS will require further studies. Additionally, it will be crucial to assess whether inhibition of HuR constitutes a viable therapeutic strategy. A potential limitation is the reduced efficacy of this approach in EwS cells with low expression of the EWSR1::FLI1 fusion protein. Such cells are thought to contribute to resistance to current chemotherapies and relapse in EwS patients[42].

In conclusion, our findings redefine the molecular portray of EWSR1::FLI1 to include a function in mRNA stability. The possibility that our findings might be extended to additional fusion TFs, such as other FET::ETS fusions, not only revisits our comprehension of how oncogenic fusion TFs rewire gene expression but also opens new therapeutic avenues for these difficult-to-target chimeras.

Methods

Ethical statement

Mouse studies were approved by the government of North Baden as the responsible legal authority (permit number G-3/20), and adhered to the ARRIVE guidelines, European Community, and UKCCCR.

Cell lines and cell culture

A673, HeLa, HEK293T, MCF7, MDA-MD-231 and U2OS cells were purchased from American Type Culture Collection (ATCC) and were not further authenticated upon receipt. Ewing sarcoma cell lines expressing doxycycline (dox)-inducible shRNA against EWSR1::FLI1, shA673-1c and shSK-E17T, were a generous gift from Dr. Olivier Delattre (Institut Curie, Paris) and have been described previously[42]. The TC71 and MHH-ES1 EwS cell lines were obtained from the German Collection of Microorganisms and Cell cultures (DSMZ) and Dr. Thomas Grünewald (DKFZ, Heidelberg), respectively. Ewing sarcoma cell lines were not further authenticated upon receipt but the presence of the expected EWSR1::FLI1 fusion was validated by RNA-sequencing and western blotting. Bone marrow-derived human mesenchymal stem cells (hMSC) were kindly provided by Dr. Yves Beguin (CHU, Sart-Tilman). All cells were cultured in a 37 °C 5% CO_2 humidified incubator with medium supplemented with 10% FBS (Gibco) and 1% Penn/Strep (Biowest). HeLa, HEK293T, MCF7, MDA-MD-231 and shSK-E17T were maintained in DMEM high glucose (Biowest), U2OS in McCoy's 5 A Medium (Lonza), shA673-1c in DMEM high glucose with 20 μg/ml blasticidin (InvivoGen) and 200 μg/ml zeocyn (InvivoGen), TC71 in IMDM (Gibco), and MHH-ES1 in RPMI1640 with L-glutamine (Biowest). Primary cells with passages between 2 and 5 were used for all experiments. All cell lines were monthly checked for mycoplasma by MycoAlert™ Mycoplasma Detection Kit (Lonza).

Establishment of A673 KD/rescue cell lines

For KD/rescue experiments, shRNA targeting the 3′UTR of EWSR1::FLI1 was cloned into the pLV[miR30]-Puro-TRE > EGFP vector (Vector Builder). The shRNA target sequence is described in Supplementary Data 3. Lentivirus production was performed in HEK-293T cells. A673 EwS cell line (ATCC) was first transduced with TET3G (MOI = 50) and selected with 100 μg/ml hygromycin B (InvivoGen). Next, cells were subjected to 2 rounds of infection (MOI = 100) with EWSR1::FLI1 3′UTR shRNA and selected with 1 μg/ml puromycin (InvivoGen). Single-cell cloning was performed and the A673-shEF3′.11 clone was selected based on knockdown efficacy, as assessed by western blot analysis after dox treatment (1 μg/ml for 4 days). For rescue expression, ORF coding for FLAG-tagged full-length EWSR1::FLI1 or Δ63EWSR1::FLI1 were delivered into dox-treated A673-shEF3′.11 clone by lentiviral infection (see Lentiviral vector transductions section below) and cells were selected with 10 μg/ml blasticidin.

Plasmids

Open reading frames (ORFs) encoding human *EWSR1, FLI1* and subunits of CCR4-NOT and PAN2-PAN3 deadenylation complexes were obtained as pDONR223 from the human ORFeome v7.1 and v8.1 (The Center for Cancer Systems Biology, Dana-Farber Cancer Institute, CCSB-DFCI). HA-tagged CNOT3, CNOT6 and CNOT7 were kindly provided by Dr. Elisa Izaurralde (European Molecular Biology Laboratory, Heidelberg, Germany). Myc-tagged CNOT2 deletion mutants were described previously[35]. *R-Luc-8MS2*, *R-Luc-0MS2*, *R-Luc-8AU* and *R-Luc-0AU* reporter constructs were described previously[55]. Destination vectors used in this study include: pDEST1899 (FLAG N-terminal tag), pCS3MTdest (Myc N-terminal tag, Addgene), pDEST475 (HA N-terminal tag, Invitrogen), pGLucN1 or pGLucN2 (Gaussia luciferase fragment 1 or 2 N-terminal tag)[59] and pDEST-EGFP (EGFP-N-terminal tag, Addgene). All plasmids used in this study are listed in Supplementary Data 3.

Cloning

The most frequent splicing variant of *EWSR1::FLI1* (i.e., between exon 7 of EWSR1 and exon 6 of FLI1) was used in all experiments. *EWSR1::FLI1* 7/6 gene fusion was generated from pDONR223-EWSR1 and pDONR223-FLI1 using PCR-fusion/Gateway cloning procedure as described previously[106]. *ΔETS-EWSR1::FLI1* contains a deletion of 65 aa in its ETS domain and was described elsewhere[66,67]. It was generated from full-length *EWSR1::FLI1* using PCR-fusion/Gateway cloning procedure. *YS37EWSR1::FLI1* was synthesized by Integrated DNA Technologies (IDT) company. In this construct, all 37 tyrosines from the low-complexity N-terminal domain of EWSR1 (aa 1-264) were replaced by serines. SAGQQS, SIGQQS and SFGQQS tyrosine mutants of EWSR1 low-complexity N-ter region have been described previously[63]. In these constructs, the first 17 tyrosines within DHRs were replaced by alanine (A), isoleucine (I) or phenylalanines (F), respectively. EWSR1::FLI1 7/6, ΔETS-EWSR1::FLI1, EWS:FLI1ΔCTAD, Δ63EWSR1::FLI1, EWSR1-Nter, FLI1-Cter, YS37EWSR1::FLI1, SAGQQS, SIGQQS, SFGQQS and deletion mutants of EWSR1 low-complexity region were inserted into pDONR223 by BP cloning (Gateway recombination technology, Invitrogen) with specific primers flanked at the 5′site by the following AttB1 and AttB2 Gateway sites: 5′-GGGGACAACTTTGTACAAAAAAGTTGGC(ATG)−3′ (AttB1) and 5′-GGGGACAACTTTGTACAAGAAAGTTGA-3′ (AttB2). Inserts from pDONR223 were subsequently transferred by LR cloning (Invitrogen) into destination vectors described in the above section depending on the needs[35,55]. For the tethering degradation assay (see below), pDEST1899 Flag-tagged ORFs were subcloned in the pN-MS2-CP (MS2 N-terminal tag, described previously[107] following classical cloning procedure. For GGAA reporter assays, a pGL3-GGAA-*Firefly* reporter construct was generated by inserting 12 GGAA repeats between the SacI and XhoI restriction sites upstream the SV40 promoter of the pGL3-*Firefly* vector (Addgene). Sequences of the GGAA oligonucleotides are available in Supplementary Data 4.

Lentiviral constructs encoding CTL and HuR shRNA were generated by inserting oligonucleotides (CTRL: 5′-GCAGTTATCTGGAAGATCAGGTTGGATCCAACCTGATCTTCCAGATAACTGC-3′; HuR: 5′-AAAAGGGAATGGACCAAAGAGTTTCTTGGATCCAAGAAACTCTTTGGTCCATTCCC-3′) in the pLV-H1alpha-puro plasmid (Biosettia) according to the manufacturer's instructions.

The sequences encoding human HuR and HuR RRM1, RRM3 and deletion mutants were generated by PCR and inserted in the EcoRI site of the pcDNA3.1-mcherry[108]. All the constructs were verified by sequencing and maps are available upon reasonable request.

For lentivirus-based overexpression, a pLENTI-DEST vector was generated by transferring the insert from the pDEST1899 backbone vector into a pLENTI purchased from GenScript using XhoI restriction sites. All constructs were verified by sequencing at the GIGA-Genomics facility (University of Liège, Belgium). All cloning and sequencing primers are listed in Supplementary Data 4. All plasmids generated by cloning in this study are listed in Supplementary Data 3. Additional information about plasmids is available upon reasonable request.

Chemicals

For mRNA decay experiments, cells were treated with 5 μM Actinomycin D (ActD) for up to 4 or 8 h to block transcription. Inhibitors of HuR, dihydrotanshinone-I (DHTS) and CMLD-2[80,81,109] were respectively purchased from Sigma-Aldrich and MedChemExpress. All chemicals used in this study were dissolved in DMSO (Carl Roth, A994.1).

DNA and siRNA transfection

For the tethering degradation assay and 12xGGAA reporter assay, HeLa cells were transfected with polyethyleneimine (PEI) using 1:2 DNA/PEI ratio. For the Gaussia Protein Complementation Assay (gPCA) and for co-immunoprecipitations, HEK293T cells were used and transfected with PEI or with a classical calcium phosphate procedure, respectively. For transient knockdown of CNOT2, siRNAs were purchased from Eurogentec (Belgium). Sequence of the CNOT2 siRNA is available in Supplementary Data 3. Transfection of siRNA or DNA in HeLa or shA673-1c cells were performed using JetPrime (Polyplus transfection) according to the manufacturer's instructions. Cells were processed at 24–48 h or 72 h after DNA or siRNA transfections, respectively.

Lentiviral vector transductions

For stable ectopic expression studies, FLAG-tagged EWSR1::FLI1 wild-type or mutants were cloned into the XhoI sites of the pLENTI-DEST vector. The recombinant lentiviral constructs were delivered in hMSCs or shA673-1c cells after KD of endogenous EWSR1::FLI1. Lentivirus were prepared at the GIGA-Viral Vectors facility (University of Liege, Belgium). Cells were transduced (MOI = 100) with protamine sulfate. After 72 h, cells were treated for 72 h with 7 μg/ml blasticidin and then amplified for 2 weeks. Expression of a EWSR1::FLI1 breakpoint-specific shRNA in shA673-1c and shSK-E17T cells was performed by adding 1 μg/ml of doxycycline (dox) in the medium *ex-tempo*, as previously described[41,42]. shA673-1c and shSK-E17T cells were processed after 4 days or 7 days of dox treatment, respectively. For stable KD of HuR, shRNA constructs were prepared for lentivirus delivery and shA673-1c cells were transduced (MOI = 20) as described above. Cells were subsequently processed or selected with 3 μg/ml puromycin for 72 h. shRNAs used in this study are listed in Supplementary Data 3.

Western blotting

Cells were washed once with cold PBS, collected by trypsinization and centrifugation. Total cell lysate was prepared by directly lysing the cell pellet in Laemmli buffer, ultrasonication when necessary, and boiling for 5 min at 100 °C. Protein extracts were separated by sodium dodecyl sulfate-polyacrylamide gel (SDS-PAGE) electrophoresis and transferred onto nitrocellulose membrane. Membranes were blocked for 1 h with 5% non-fat milk or 4% BSA and incubated overnight at 4 °C with primary antibodies followed by HRP-conjugated secondary antibodies (1:4000 dilution). Proteins were detected by chemiluminescence. Images were acquired with ImageQuant LAS 4000 device (GE Healthcare) and quantified using ImageJ when relevant. All primary antibodies used for western blotting are listed with working dilutions in Supplementary Data 5.

RNA isolation and quantitative PCR

For expression studies and mRNA decay analyses, RNA was isolated using the Nucleospin RNA kit (Macherey-Nagel) according to manufacturer's instructions. For RNA-immunoprecipitations, total RNA was extracted from inputs or beads with TRIzol Reagent (Thermo Fisher Scientific). After isolation and quantification with a Nanodrop instrument (Thermo Fisher Scientific), RNA was reverse-transcribed with random primers using the RevertAid H Minus First Strand cDNA Synthesis Kit (Thermo Fisher Scientific). cDNA was diluted between 10- and 300-fold depending on the abundance of targets, amplified using FastStart SYBR Green Master mix (Roche) on a LightCycler 480 instrument (Roche). Experiments were carried out in triplicate for each data point and final results are presented as average of at least 3 biological replicates. Relative quantification of targets, normalized to an endogenous control, was performed using the comparative ΔΔCt method. Using this method, we obtained the fold changes in gene expression or enrichment, normalized to an internal control (*GAPDH* for gene expression levels) or to input (for RIP experiments). For mRNA decay analyses, qPCR signals were normalized to the average levels of three highly stable mRNAs (*GAPDH*, *RPL32* and *NDUFA12*), and half-lives were calculated based on first-order degradation kinetics. HPLC-purified oligonucleotides were purchased from Eurogentec. Primer specificities were evaluated in silico using a blast homology search and assessed post-amplification by examination of the melt curve. Primer efficiencies were evaluated by the PCR standard curve method and only primers with > 98% efficiency were used. Sequences of qRT-PCR primers can be found in Supplementary Data 6.

Genome-wide mRNA decay with ActD-RNA-seq

Biological replicates of shA673-1c cells before (-dox) and after (+dox) knockdown of EWSR1::FLI1 were seeded at day 4 of dox treatment in 6-well plates and treated with 5 μM ActD for 0, 1, 2 and 4 h. Total RNA was harvested and RNA quality was assessed using BioAnalyzer. Libraries were prepared with the Illumina TruSeq stranded mRNA sample preparation kit (with oligo(dT) selection step) and single-end sequencing was performed with the Illumina NextSeq 500 instrument by the GIGA-Genomics facility (University of Liege, Belgium). RNA-seq read quality was evaluated using FastQC. Sequence reads were aligned to the human genome hg19 (UCSC) using STAR[109,110]. Computing of mRNA HLs was performed on read counts at 0, 1, 2 and 4 h time points from STAR quant Mode using R package bridger2 (https://CRAN.R-project.org/package=bridger2). Assuming first-order decay kinetics (see Eq. 1), mRNA half-lives (HLs) were calculated as the ratio between ln2 and the decay constant rate k (see Eq. 2).

$$M = M_0.e^{-k.t} \quad (1)$$

where M_0 is the initial mRNA abundance, i.e., before decay starts (0 h time point).

$$t_{1/2} = \frac{\ln 2}{k} \quad (2)$$

Genes with low mean expression levels (< 100 read counts) in the control condition were removed from this analysis. Bridger2 outputs were used to compute half-life ratio between −dox and +dox conditions. mRNAs were considered significantly stabilized or destabilized if their absolute HL ratio was > 1 (i.e., absolute log2(HL) ratio > 0) and their *p*-value (unadjusted) < 0.05 using two-sided paired Student's *t*-test. Highly stable mRNAs with HL > 24 h in the −dox condition were removed from the output results. For qPCR-based mRNA decay experiments, cells were seeded in 6-well or 12-well plates and treated with 5 μM ActD for up to 4 or 8 h. Total RNA was extracted, reverse-transcribed and HLs were calculated based on first-order degradation

kinetics with GraphPad Prism 8. Volcano plot and heatmaps presented in this study were generated using GraphPad Prism 8.

Differential gene expression analysis

Genes differentially expressed upon EWSR1::FLI1 knockdown in shA673-1c cells were identified with DESeq2[111] (10.18129/B9.bioc.DESeq2) on time point 0 h (untreated) of the ActD kinetics by comparing EWSR1::FLI1^{high} (-dox) to EWSR1::FLI1^{low} (+dox) cells. Only protein-coding genes were kept. Genes were considered significantly up- or down-regulated if their $\log_2$ fold change was > 1 or < −1 and their adjusted *p*-value was < 0.01.

Genome-wide mRNA decay using DiffRAC analysis

STAR-aligned reads to the genome upon EWSR1::FLI1 KD in shA673-1c (GSE164372) and TC-32 cell lines (GSE243184) were quantified using the *Counting Reads for Intronic and Exonic Segments (CRIES)* pipeline (https://github.com/csglab/CRIES)[46]. Briefly, this pipeline allows the selective quantification of RNA-seq reads to introns and exons of every gene using HTSeq 1.99.2[110] based on annotation tables derived from Ensembl GRCh38 version 103 using HISAT2 2.1.0[112]. Intronic and exonic read counts were then used as input for the Differential Ratio Analysis in Count data (DiffRAC) analysis using R[33]. All data processing was performed using R.

Metabolic labeling with 4-Thiouracil (4sU), qPCR and analysis

Biological replicates of shA673-1c cells before (-dox) and after (+dox) knockdown of EWSR1::FLI1 were seeded in 6 well-plates. Cells were incubated with 400 μM of 4sU to label newly transcribed mRNAs and harvested after 0, 1, 2 and 4 h. Cells were washed once with cold PBS before isolation of total RNA with Nucleospin RNA kit (Macherey-Nagel). After isolation and quantification using a Nanodrop instrument (Implen), 500 ng of RNA was treated with 3 μL of a N-ethylmaleimide (NEM) solution at 50 μg/μL to covalently modify 4sU and interfere with the reverse transcription of 4sU-labeled mRNA. After NEM labeling, RNA was purified using RNA Clean and Concentrator 5 spin columns kit (Zymo) according to manufacturer instructions. Purified RNA was reverse-transcribed using the cDNA FastGene® Scriptase II kit with oligo-d(T) primers (Nippon Genetics) and diluted between 10- to 20-fold. Real time quantitative PCR reactions were performed in triplicate using FastStart SYBR Green Master mix (Roche) on a LightCycler 480 instrument (Roche) to monitor decreasing levels of 4sU-unlabeled mRNAs. Relative gene expression was calculated using the ΔΔCt method and normalized to *GAPDH*, *NDUFA12* and *RPL32* mRNAs for each timepoint. The qPCR primers were designed using the NCBI Primer-Blast tool to specifically target the 3' end of the target mRNAs. Sequences of primers used for 4SU-qPCR can be found in Supplementary 6.

Luciferase reporter assays

Luciferase MS2-tethering mRNA stability assays were performed in HeLa cells as described elsewhere[35]. Briefly, cells were transfected with control MS2-CP or various MS2-CP-tagged constructs, together with a bidirectional reporter encoding a control *Firefly* luciferase (F-Luc) and a targeted *Renilla* luciferase carrying 8 (8MS2) or lacking (0MS2) repeats of the binding sequence for the MS2 coating peptide in its 3'UTR (*R-Luc-8MS2* and *R-Luc-0MS2*, respectively)[55]. Luciferase ARE-tethering assays were performed in shA673-1c cells previously treated or not with dox. Briefly, cells were transfected with control pCDNA3.1-mCherry empty vector or pCDNA3.1-mCherry-HuR vector, together with a bidirectional reporter encoding a control *Firefly* luciferase (F-Luc) and a targeted *Renilla* luciferase (R-Luc) carrying or lacking 8 repeats of AU-rich elements (AREs) in its 3'UTR (*R-Luc-8AU* and *R-Luc-0AU*, respectively)[55]. For GGAA reporter assays, HeLa cells were transfected with pGL3-GGAA-Firefly vector and various FLAG-tagged constructs, together with pRL-SV40 vector (Promega) to normalize for differences in cell counts and transfection efficacies. For measuring luciferase activities in all these assays, cell lysis and luciferase assays were performed in triplicate on a TriStar² S LB 942 luminometer (Berthold) with twinlite *Firely* and *Renilla* Luciferase Reporter Gene Assay System (Perkin Elmer).

SMN2-MS2 minigene assay

SMN2-MS2 minigene assays were performed using HeLa cells co-transfected with either control empty vectors, or various FLAG- or MS2-CP-tagged constructs, together with SMN2-MS2 minigene described elsewhere[72,76]. After 48 h following transfection, cells were washed twice with PBS and harvested on ice. A third of the sample was saved for subsequent western blotting analysis. Total RNA was isolated from the remaining amount of sample, treated with DNAse I (Thermo Fisher Scientific) for 30 min at 37 °C, and reverse-transcribed following DNAse I inactivation. Next, RT-PCR amplifications were performed using forward and reverse primers of SMN2-MS2 minigene located within exon 6 and exon 8, respectively (sequences of SMN2 primers can be found in Supplementary Data 6). Then, PCR products were resolved by electrophoresis on a 12% polyacrylamide gel at 180 V for 1 h. Gels were incubated with GelStar™ fluorescent stain (Lonza) 1:10 000 in a Tris-Borate-EDTA buffer under gentle agitation for 25 min and washed twice with dH_2O. Fluorescence was recorded using the Amarsham ImageQuant 800 (Cytiva) camera. Density analysis of the bands in the acquired images was performed using the ImageQuant TL software (v. 7). Percent spliced in (PSI) were computed based on the ratio between the densitometry values of the long isoform and all isoforms.

Gaussia protein complementation assay (gPCA)

ORFs encoding subunits of CCR4-NOT and PAN2-PAN3 deadenylation complexes, as well as EWSR1::FLI1 full-length, domains and deletion/tyrosine mutants were cloned into destination vectors containing GlucN1 and GlucN2 fragments of the *Gaussia princeps* luciferase[59]. HEK293T cells were seeded in 24-well plates and transfected with 500 ng of the appropriate constructs (GlucN1 + GlucN2), respectively. After 24 h, cells were washed with PBS and lysed in 200 μL using the Renilla Luciferase Kit (Promega) according to manufacturer's instructions. Twenty μL of lysates were then used to quantify luminescence in triplicate on a TriStar² S LB 942 luminometer (Berthold). The remaining volume of lysate was mixed with Laemmli buffer for SDS-PAGE analysis and western blotting. Positive and negative interactions were defined using a One sample *t*-test against the value of 3.5 (with hypothesis set to"greater") as recommended previously[59].

Immunofluorescence and confocal microscopy

HeLa, shA673-1c and shSK-E17T cells were seeded on coverslips in 24-well plates. Cells were washed with warm PBS and fixed in warm PBS with 4% paraformaldehyde (PAF) for 15 min. Cells were then washed in PBS, permeabilized in PBS with 0.5% Triton X-100 for 10 min and incubated in blocking solution (PBS with 0.025% Tween- 20 and 10% FBS) for 1 h. The coverslips were then incubated overnight with primary antibodies and Alexa-conjugated secondary antibody for 1 h in blocking solution. Nuclei were counterstained with DAPI (Life Technologies, 1:10,000 in PBS) for 10 min at room temperature in the dark and washed three times for 5 min each with PBS. The coverslips were mounted onto microscope slides with ProLong™ Diamond Antifade Mountant (Invitrogen). Images were obtained with a Zeiss HR LSM Airyscan 880 confocal microscope using a 40x or 63x oil immersion objective at GIGA-Imaging facility (University of Liege), visualized and analyzed with Fiji (ImageJ) software. P-bodies (PBs) counting was performed on cells reconstituted in 3D with IMARIS v9.5.1 software. Surfaces were constructed from DCP1A and EDC4 labeling, considering fluorescence signals above a control threshold, and were filtered for a minimum volume of 0.01 μm^3 or 0.1 μm^3, respectively. PBs were counted using the IMARIS software. Cell number was determined

based on the DAPI signal, and the mean number of PBs per cell was calculated as the ratio between the total number of PBs in a field and the total number of nuclei in the same field. All antibodies used for immunofluorescence are listed with dilutions in Supplementary Data 5.

Proximity ligation assay

U2OS cells were transfected with Myc-HuR and FLAG-EWSR1::FLI1 or FLAG empty vector, and fixed with a solution of 4% PFA. After extensive washes with PBS, we used a Duolink® kit (Sigma-Aldrich, DUO92191) to perform the experiments following the company instructions. Here, we used a mouse anti-FLAG (Sigma-Aldrich, F3165) and a rabbit anti-MYC (Santa Cruz, sc-789) antibody. Images were acquired on a Yokogawa CV7000 microscope and analyzed with a custom ImageJ pipeline separating interacting signal of the nucleus from the cytoplasmic area. The number of cells analyzed is indicated in the figure legend.

Co-immunoprecipitation (co-IP)

HEK293T cells coexpressing tagged interaction partners were lysed in IPLS (immunoprecipitation low salt; Tris-HCl, pH 7.5 50 mM, EDTA, pH 8, 0.5 mM, 0.5% NP-40, 10% glycerol, 120 mM NaCl) with 1x cOmplete Protease Inhibitor (Roche) and 1x Halt Phosphatase Inhibitors (Thermo Fisher Scientific). When necessary, cleared cell lysates were incubated at 37 °C for 30 min with or without 10 μg/ml Rnase A (Thermo Fisher Scientific). Negative control was cells transfected with control FLAG empty-vector (-). Supernatants were then incubated with anti-FLAG M2 agarose beads (Sigma-Aldrich) for 2 h at 4 °C. Beads were washed once with IPLS, twice with IPMS (immunoprecipitation medium salt, IPLS with 500 mM NaCl) and once with IPLS. Immunoprecipitates were finally boiled in 2x SDS Laemmli buffer and subsequently analyzed by SDS-PAGE and western blotting. For endogenous co-IP, shA673-1c cell lysates were prepared with a modified IPLS-HEPES buffer (50 mM HEPES-NaOH, pH 7.4, instead of Tris buffer), precleared with Protein A/G magnetic beads (Millipore) for 1 h at 4 °C, and incubated overnight with 1 μg of relevant antibody or normal rabbit (Cell Signaling) or mouse (Santa Cruz) IgG. Then, samples were incubated with Protein A/G magnetic beads (Millipore) for 1 h at 4 °C. Beads were washed four times with IPLS-HEPES buffer. Immunoprecipitates were finally boiled in 2x SDS Laemmli buffer and analyzed by SDS–PAGE and western blotting. Antibodies used for co-IP are listed with quantities in Supplementary Data 5.

Biotinylated isoxazole precipitation

These experiments were performed as previously described[68] with slight modifications. Biotinylated isoxazole (b-isox, Sigma-Aldrich) was dissolved in DMSO. Briefly, cells collected from one 10 cm dish were resuspended in 1 ml lysis buffer (20 mM Tris-HCl pH 7.4, 150 mM NaCl, 5 mM MgCl2, 0.5% NP-40 and 10% glycerol supplemented with 1X Protease/Phosphatase inhibitors (Pierce), 0.1 mM PMSF and 20 mM beta-mercaptoethanol) and incubated for 30 min at 4 °C with rotation. Next, protein supernatant was collected after centrifugation for 15 min at 18,000 x g 4 °C, and treated with 100 mg/ml RNAse A (Thermo Fisher Scientific) for 30 min at 37 °C. A 5% whole cell extract (WCE) control was saved and the remaining proteins were divided into four aliquots before addition of b-isox at 0, 10, 30, 100 μM final concentrations. The aliquots were then incubated for 1 h at 4 °C with rotation and centrifuged for 15 min at 18,000 x g + 4 °C. Supernatant was saved for further analysis and pellets were washed twice in supplemented Lysis buffer before resuspension in Laemmli buffer. WCE, pellets and supernatants were analyzed by SDS–PAGE on 10% gels and western blotting.

RNA-immunoprecipitation-qPCR analysis

Dynabeads Protein G magnetic beads (Invitrogen) were incubated with anti-FLI1 antibody (ab15289, Abcam), anti-HuR antibody (sc-5261, Santa Cruz), normal rabbit (Cell Signaling) or mouse IgG (Santa Cruz) at 4 °C overnight with rotation. Cells were washed twice with ice cold PBS and pelleted by centrifugation (4 °C, 5 min, 250 x g). Cells were resuspended in 1 ml RIPA (50 mM Tris HCl, pH 8.0, 150 mM NaCl, 1.0% IGEPAL CA-630, 0.5% sodium deoxycholate, 0.1% SDS) with 1x cOmplete Protease Inhibitor (Roche) and lysed for 30 min at 4 °C with rotation. Cell lysates were then sonicated on ice with a pulser mode (3x 30 s with 30 s break each) and cleared by centrifugation for 10 min at 4 °C and at 10,000 x g. Proteins were quantified with Pierce BCA protein assay kit (Thermo Fisher Scientific). An aliquot (~ 40 μg) was saved for RNA input and stored at −20 °C. For immunoprecipitation, 400 μg of protein were incubated with antibody-loaded Dynabeads overnight at 4 °C with rotation. Supernatant was removed and beads were washed 5 times with 1 ml RIPA buffer. RNA-protein complexes were then eluted by incubation with 100 μL of elution buffer (Tris–HCl pH 8 100 mM; Na2-EDTA 10 mM; 1% SDS in H_2O) for 3 min at 90 °C. An aliquot (10 μl) was saved for western blotting analysis. Proteins from RNA inputs or beads were digested with 200 μg/ml Proteinase K treatment (37 °C for 1 h and 70 °C for 45 min) and RNA was extracted with TRIzol Reagent (Thermo Fisher Scientific). cDNA was reverse-transcribed using the RevertAid H Minus First Strand cDNA Synthesis Kit (Thermo Fisher Scientific) and diluted 10-fold prior to qPCR analysis. RIP enrichment was calculated as a percentage of input. The GAPDH, NDUFA12 or RPL32 mRNAs were used as controls. All primers used for RIP experiments are listed in Supplementary Data 6.

RNA-binding motif enrichment analysis

Target 3'UTR and non-target 3'UTR sequences were retrieved using biomaRt R package (10.18129/B9.bioc.biomaRt). In the ActD-RNAseq analysis of shA673-1c cells, 746 target 3'UTR sequences (746/772; ~97%) and 6,215 non-target 3'UTR sequences (6,215/6,372; ~98%) were retrieved. In the DiffRAC analysis of shA673-1c and TC-32 cells, 893 common target 3'UTR sequences were retrieved. The FASTA files generated for target 3'UTR sequences were then interrogated for known RNA-binding motifs using the AME software from MEME suite 5.0.2 with default settings[113]. Motifs with an adjusted p-value < 0.05 were considered significant. Control sequences consisted of the 3'UTR region of transcripts with unchanged HL ratio before and after knockdown of EWSR1::FLI1 (i.e., non-target 3'UTRs). Alternatively, the built-in control provided by the MEME suite was also used.

Heptamer enrichment analysis

All possible heptamers were generated using the *crossing* function from tidyr R package. Next, individual heptamers were counted in target and non-target 3'UTR sequences from the ActD-RNA-seq analysis of shA673-1c cells. Counts were expressed per kb of sequence length. For each heptamer, the difference in count between target and non-target 3'UTRs was calculated and standardized using Z-score transformation. Two-tailed p-values were computed and adjusted for multiple testing using the Bonferroni method. These adjusted p-values were used to indicate the significance of enrichment.

Investigation of intrinsic disorder properties

Eight algorithms were used with default settings: IUPRED2[114], VL3[115], RONN[116], SPOT-Disorder[117], AUCPred[118], ESpritz[119], Metadisorder[120], and POODLE[121]. Results are shown as mean disorder scores from these algorithms.

Docking and molecular dynamics

The FLI1-derived region of EWSR1::FLI1 7/6 protein (residues 220 to 452 from UniProt entry Q01543) and the full-length HuR protein (UniProt entry Q15717) structure were retrieved from the AlphaFold Protein Structure Database[122,123]. The carboxy-terminal activating domain (CTAD) of FLI1 (residues 362 to 452) was not predicted to form any stable secondary structures or intramolecular bonds. AlphaFold prediction suggested a very high-confidence structure (pLDDT > 90) of the RRM3 domain of HuR forming four short β-sheets interspaced with two α-

helices. The predicted structure showed a strong similarity with crystal structures of sub-domains of HuR retrieved from the Protein Data Bank entries 6GD2, 6GD3, and 6G2K[124]. Both chains were subjected to molecular docking using the HADDOCK2.4 web server[125] with default parameters, with the CTAD domain and the RRM3 indicated as ambiguous interaction restraints based on experimental data. The resulting docking structure with the highest confidence score from cluster 1 was then retrieved and subjected to a molecular dynamics (MD) simulation using GROMACS 2020.4[126,127]. The main interacting amino acids suggested by molecular docking along with short flanking regions, i.e., residues 321 to 446 of FLI1 and residues 220 to 323 of HuR, were introduced in the system. The system topology was generated using the CHARMM36 all-atom force field[128] in a dodecahedron box and solvated with 54,902 water molecules in a SPC/E water model. The system was further neutralized by the addition of 8 Cl^- ions. Energy minimization of the resulting structure was carried out using the steepest descent algorithm with a target maximum force of under 1000 kJ/mol. Subsequently, two stages of equilibration were performed for 100 ps each. The first equilibration step at a temperature of 300 K was conducted under a constant Number of particles, Volume, and Temperature (NVT) ensemble, while the second equilibration step was conducted under a constant Number of particles, Pressure, and Temperature (NPT) ensemble at a target pressure value of 1 bar. The equilibrated system was finally subjected to the production MD for 250 million steps with a time-step of 2 fs, resulting in a total 500 ns simulation duration. Post-processing of simulation and analysis were performed using GROMACS and VMD 1.9.4a55[129]. Final representation was generated using PyMOL 2.5.

Number & Brightness (N&B) analysis

U2OS cells were transiently transfected with JetPrime for the indicated N-EGFP-tagged or mGR-N525-EGFP constructs, the latest being used as monomeric control. After 24 h, images were taken using an LSM 780 laser scanning microscope (Carl Zeiss, Inc.) equipped with an environmental chamber. We used a 63× oil immersion objective (N.A. = 1.4). The excitation source was a multiline Ar laser tuned at 488 nm. Fluorescence was detected with a gallium arsenide phosphide (GaAsP) detector in photon-counting mode. N&B measurements were done as previously described[71]. Briefly, for each studied cell, a single-plane stack of 150 images (256 × 256 pixels) was taken in the conditions mentioned above, setting the pixel size to 80 nm and the pixel dwell time to 6.3 µs. In every case, we discarded the first 10 images of the sequence to reduce overall bleaching. The frame time under these conditions is 0.97 s. Each stack was further analyzed using the N&B routine of the "GLOBALS for Images" program developed at the Laboratory for Fluorescence Dynamics (University of California, Irvine, CA). The experiments were independently repeated two to three times for each treatment/condition.

Survival analysis

Kaplan-Meier survival analyses were carried out in 166 EwS patients, whose molecularly confirmed and retrospectively collected primary tumors were profiled at the mRNA level by gene expression microarrays in previous studies[85–88]. To that end, microarray data generated on Affymetrix HG-U133Plus2.0 or Affymetrix HuEx-1.0-st microarrays of the 166 EwS tumors (Gene Expression Omnibus (GEO) accession codes: GSE63157[85], GSE12102[86], GSE17618[87], GSE34620[88] provided with clinical annotations were normalized separately as previously described[130]. Only genes that were represented on all microarray platforms were kept for further analysis. Batch effects were removed using the ComBat algorithm[131]. Data processing was done in R.

Viability assays

Cells were seeded in triplicate at a density of 5,000–20,000 cells per well of a 96-well plate (Corning, Costar black clear bottom). After 24 h, cells were treated with various concentrations of DHTS or CMDL-2, or 1% DMSO as control (vehicle). After 24 h, the medium was removed and cells were incubated with resazurin (Stemcell Technologies) for 2–4 h. Finally, fluorescence was recorded at the excitation and emission wavelengths of 535/595 nm with a FiterMax F5 microplate reader (Molecular Devices). Quantifications were done on 3 independent replicates.

2D-clonogenic assays

shA673-1c cells were resuspended in 0.3% of top agar and seeded in duplicate at a density of 8,000 cells per well of a 12-well plate with 0.6% bottom agar. If needed, cells were then treated with varying doses of DHTS or CMLD-2 inhibitors. Plates were incubated in a cell culture incubator (37 °C, 5% CO_2) for 3 weeks. Colonies were stained with crystal violet (0.1% crystal violet, 20% methanol, in dH_2O) for 30 min, washed four times with dH_2O, imaged with a Nikon D3200 and finally counted using ImageJ. Quantifications were done on 2 to 4 independent replicates.

Wound healing migration assays

Three biological replicates of shA673-1c cells were seeded at a density of 20,000 cells per well of a 96-well plate. At cell confluence, scratch wounds were produced using a WoundMaker device (Essen Bioscience). Cells were next treated with 1 or 2 µM of DHTS, or vehicle. Following treatment, cell migration into the wound was monitored every 2 h for 24 h and analyzed by time-lapse microscopy (IncuCyte S3, Essen Bioscience, Sartorius, wound mode, 10x objective lens).

3D-spheroid growth assays

Spheroids were formed in 96-well plates (Greiner, flat bottoms) previously coated with 1% agar prepared in dH_2O and sterilized by autoclaving. shA673-1c cells were seeded at a density of 5,000 cells per well in duplicates in DMEM supplemented with 2% FBS. If needed, cells were treated with varying doses of DHTS or CMLD-2 inhibitors (1% DMSO as control) with or without 20 nM SYTOX Green (ThermoFisher Scientific) directly after seeding or once spheroids were formed. Spheroid growth was monitored every 2 h for 96 h and analyzed by time-lapse microscopy (IncuCyte SX5, Essen Bioscience, Sartorius, spheroid mode, 4x objective lens). Quantifications were done on 4 to 6 independent replicates.

In vivo tumor growth analysis

Three experimental groups of 8 animals each, corresponding to A673-shEF3'.11 rescued with control FLAG empty vector, full-length EWSR1::FLI1 or Δ63EWSR1::FLI1 were used. One million cells diluted in 50% PBS and 50% Matrigel were subcutaneously injected in the right flanks of NSG mice. Animals received dox in the drinking water since 24 h prior to the subcutaneous injection, and subsequently every day until the end of the experiment. The tumors were measured with a caliper every ca. 2 days and tumor growth was recorded accordingly. One of the animals in the wild-type group never grew a tumor and was excluded from the analysis. Once animals reached termination criteria, they were sacrificed, and the tumors were extracted and weighted. Experiments were approved by the government of North Baden and conducted in accordance with ARRIVE guidelines and recommendations of the European Community (86/609/EEC) and UKCCCR (guidelines for the welfare and use of animals in cancer research). The maximal tumor size was determined as 1000 mm^3 and it was not exceeded throughout the duration of the experiments. Housing conditions were kept as follows: food and access to water were provided ad libitum; light/dark cycle were kept in accordance to the lighting scheme for rodents (increasing transition light: 6:00 a.m.–7:00 a.m; Light phase: 7:00 a.m.–7:00 p.m; Diminishing transition light: 7:00 p.m.–8:00 p.m; Dark phase: 8:00 p.m.–6:00 a.m.) and access to housing areas was restricted during the dark period; temperature was controlled and set at 20.0–24.0 °C; humidity was set at 45.0–65.0 % relative humidity. Mouse strain was NOD-SCID gamma

(NSG), from line NOD.CgPrkdcscid Il2rgtm1WjllSzJ, and at the time of beginning of the experiment all animals were 10–12 weeks old. All mice used were males.

Statistics and reproducibility

Unless otherwise indicated, data are presented as means ± SD, calculated for at least three independent experiments. Statistical tests were performed with GraphPad Prism 8 and are indicated in each figure legends. Significances of dataset overlaps were determined with Fisher's Exact Test using GeneOverlap R package. *p*-value thresholds are depicted as follows: $*p < 0.05$; $**p < 0.01$; $***p < 0.001$; $****p < 0.0001$; *ns* = not significant. Exact *p*-values are available in the Source Data file. Illustrative images were selected from at least 2 independent experiments. All raw data are available in the Source Data file. Unless indicated, no data were excluded from the analysis.

Reporting summary

Further information on research design is available in the Nature Portfolio Reporting Summary linked to this article.

Data availability

Reagents generated in this study will be made available on request, but we may require a payment and/or a completed Materials Transfer Agreement if there is potential for commercial application. Gene expression data after treatment with ActD up to 4 h in shA673-1c cells have been deposited to GEO repository under accession number GSE198177 (-dox) and GSE231453 (+dox). Although these datasets are available from different accession numbers, they were generated concurrently using the same shA673-1c cell culture. The full list of differentially expressed genes and differentially stabilized mRNA upon EWSR1::FLI1 KD in shA673-1c cells are available in Supplementary Data 1 and Source Data, respectively. Overlapping genes in Venn plots are available in the Source Data file. The literature-curated list of decay factors (with references) used in this study is available in Supplementary Data 2. Previously published RNA-seq data used in the DiffRAC analysis are available from[132,133] and using the following accession numbers: GSE164373 (shA673-1c) and GSE243184 (TC-32). Previously published EWSR1::FLI1 ChIP-seq data and HuR PAR-CLIP data are available from[13,65,79] and using the following accession numbers: GSE61953, GSE133228 and GSE29780. Microarray data of EwS primary tumors used for survival analysis are available from[85–88] and using the following accession numbers: GSE63157, GSE12102, GSE17618 and GSE34620. Source data are provided with this paper.

Code availability

Custom R scripts used in this study are provided as Supplementary Software 1.

References

1. Lee, T. I. & Young, R. A. Transcriptional regulation and its misregulation in disease. *Cell* **152**, 1237–1251 (2013).
2. Bradner, J. E., Hnisz, D. & Young, R. A. Transcriptional addiction in Cancer. *Cell* **168**, 629–643 (2017).
3. Garraway, L. A. & Lander, E. S. Lessons from the cancer genome. *Cell* **153**, 17–37 (2013).
4. Damerell, V., Pepper, M. S. & Prince, S. Molecular mechanisms underpinning sarcomas and implications for current and future therapy. *Signal Transduct. Target Ther.* **6**, 246 (2021).
5. Perry, J. A., Seong, B. K. A. & Stegmaier, K. Biology and therapy of dominant fusion oncoproteins involving transcription factor and chromatin regulators in sarcomas. *Annu Rev. Cancer Biol.* **3**, 299–321 (2019).
6. Brien, G. L., Stegmaier, K. & Armstrong, S. A. Targeting chromatin complexes in fusion protein-driven malignancies. *Nat. Rev. Cancer* **19**, 255–269 (2019).
7. Grünewald, T. G. P. et al. Ewing sarcoma. *Nat. Rev. Dis. Prim.* **4**, 5 (2018).
8. Delattre, O. et al. Gene fusion with an ETS DNA-binding domain caused by chromosome translocation in human tumours. *Nature* **359**, 162–165 (1992).
9. Patel, M. et al. Tumor-specific retargeting of an oncogenic transcription factor chimera results in dysregulation of chromatin and transcription. *Genome Res.* **22**, 259–270 (2012).
10. Gangwal, K. et al. Microsatellites as EWS/FLI response elements in Ewing's sarcoma. *Proc. Natl. Acad. Sci. USA* **105**, 10149–10154 (2008).
11. Tomazou, E. M. et al. Epigenome mapping reveals distinct modes of gene regulation and widespread enhancer reprogramming by the oncogenic fusion protein EWS-FLI1. *Cell Rep.* **10**, 1082–1095 (2015).
12. Sheffield, N. C. et al. DNA methylation heterogeneity defines a disease spectrum in Ewing sarcoma. *Nat. Med* **23**, 386–395 (2017).
13. Riggi, N. et al. EWS-FLI1 utilizes divergent chromatin remodeling mechanisms to directly activate or repress enhancer elements in Ewing sarcoma. *Cancer Cell* **26**, 668–681 (2014).
14. Song, J., Ng, S. C., Tompa, P., Lee, K. A. W. & Chan, H. S. Polycation-π interactions are a driving force for molecular recognition by an intrinsically disordered oncoprotein family. *PLoS Comput. Biol.* **9**, e1003239 (2013).
15. Vibert, J. et al. Oncogenic chimeric transcription factors drive tumor-specific transcription, processing, and translation of silent genomic regions. *Mol. Cell* **82**, 2458–2471.e9 (2022).
16. Barrett, C., Budhiraja, A., Parashar, V. & Batish, M. The landscape of regulatory noncoding RNAs in Ewing's sarcoma. *Biomedicines* **9**, 933 (2021).
17. Boulay, G. et al. Epigenome editing of microsatellite repeats defines tumor-specific enhancer functions and dependencies. *Genes Dev.* **32**, 1008–1019 (2018).
18. Li, M. & Chen, C.-W. Epigenetic and transcriptional signaling in Ewing sarcoma-disease etiology and therapeutic opportunities. *Biomedicines* **10**, 1325 (2022).
19. Showpnil, I. A. et al. EWS/FLI mediated reprogramming of 3D chromatin promotes an altered transcriptional state in Ewing sarcoma. *Nucleic Acids Res.* **50**, 9814–9837 (2022).
20. Sanalkumar, R. et al. Highly connected 3D chromatin networks established by an oncogenic fusion protein shape tumor cell identity. *Sci. Adv.* **9**, eabo3789 (2023).
21. Braun, K. A. & Young, E. T. Coupling mRNA synthesis and decay. *Mol. Cell Biol.* **34**, 4078–4087 (2014).
22. Haimovich, G., Choder, M., Singer, R. H. & Trcek, T. The fate of the messenger is pre-determined: a new model for regulation of gene expression. *Biochim. Biophys. Acta* **1829**, 643–653 (2013).
23. Wahle, E. & Winkler, G. S. RNA decay machines: deadenylation by the Ccr4-not and Pan2-Pan3 complexes. *Biochim. Biophys. Acta* **1829**, 561–570 (2013).
24. Raisch, T. et al. Reconstitution of recombinant human CCR4-NOT reveals molecular insights into regulated deadenylation. *Nat. Commun.* **10**, 3173 (2019).
25. Sgromo, A. et al. A CAF40-binding motif facilitates recruitment of the CCR4-NOT complex to mRNAs targeted by Drosophila Roquin. *Nat. Commun.* **8**, 14307 (2017).
26. Raisch, T. et al. Distinct modes of recruitment of the CCR4-NOT complex by Drosophila and vertebrate Nanos. *EMBO J.* **35**, 974–990 (2016).
27. Leppek, K. et al. Roquin promotes constitutive mRNA decay via a conserved class of stem-loop recognition motifs. *Cell* **153**, 869–881 (2013).
28. Sarshad, A. A. et al. Argonaute-miRNA complexes silence target mRNAs in the nucleus of mammalian stem cells. *Mol. Cell* **71**, 1040–1050.e8 (2018).

29. Solana, J. et al. The CCR4-NOT complex mediates deadenylation and degradation of stem cell mRNAs and promotes planarian stem cell differentiation. *PLoS Genet* **9**, e1004003 (2013).
30. Battich, N. et al. Sequencing metabolically labeled transcripts in single cells reveals mRNA turnover strategies. *Science* **367**, 1151–1156 (2020).
31. Krenning, L., Sonneveld, S. & Tanenbaum, M. Time-resolved single-cell sequencing identifies multiple waves of mRNA decay during the mitosis-to-G1 phase transition. *Elife* **11**, e71356 (2022).
32. Akiyama, T. & Yamamoto, T. Regulation of early lymphocyte development via mRNA decay catalyzed by the CCR4-not complex. *Front Immunol.* **12**, 715675 (2021).
33. Perron, G. et al. Pan-cancer analysis of mRNA stability for decoding tumour post-transcriptional programs. *Commun. Biol.* **5**, 851 (2022).
34. Perron, G. et al. A general framework for interrogation of mRNA stability programs identifies RNA-binding proteins that govern cancer transcriptomes. *Cell Rep.* **23**, 1639–1650 (2018).
35. Rambout, X. et al. The transcription factor ERG recruits CCR4-NOT to control mRNA decay and mitotic progression. *Nat. Struct. Mol. Biol.* **23**, 663–672 (2016).
36. Yang, C.-Y. et al. Interaction of CCR4-NOT with EBF1 regulates gene-specific transcription and mRNA stability in B lymphopoiesis. *Genes Dev.* **30**, 2310–2324 (2016).
37. Bertero, A. et al. The SMAD2/3 interactome reveals that TGFβ controls m(6)A mRNA methylation in pluripotency. *Nature* **555**, 256–259 (2018).
38. Song, T. et al. Zfp217 mediates m6A mRNA methylation to orchestrate transcriptional and post-transcriptional regulation to promote adipogenic differentiation. *Nucleic Acids Res.* **47**, 6130–6144 (2019).
39. Moon, B.-S. et al. Kruppel-like factor 4-dependent Staufen1-mediated mRNA decay regulates cortical neurogenesis. *Nat. Commun.* **9**, 401 (2018).
40. France, K. A., Anderson, J. L., Park, A. & Denny, C. T. Oncogenic fusion protein EWS/FLI1 down-regulates gene expression by both transcriptional and posttranscriptional mechanisms. *J. Biol. Chem.* **286**, 22750–22757 (2011).
41. Tirode, F. et al. Mesenchymal stem cell features of Ewing tumors. *Cancer Cell* **11**, 421–429 (2007).
42. Franzetti, G.-A. et al. Cell-to-cell heterogeneity of EWSR1-FLI1 activity determines proliferation/migration choices in Ewing sarcoma cells. *Oncogene* **36**, 3505–3514 (2017).
43. Riggi, N. et al. EWS-FLI-1 expression triggers a Ewing's sarcoma initiation program in primary human mesenchymal stem cells. *Cancer Res.* **68**, 2176–2185 (2008).
44. Watson, M., Park, Y. & Thoreen, C. Roadblock-qPCR: A simple and inexpensive strategy for targeted measurements of mRNA stability. *RNA* **27**, 335–342 (2020).
45. Gaidatzis, D., Burger, L., Florescu, M. & Stadler, M. B. Analysis of intronic and exonic reads in RNA-seq data characterizes transcriptional and post-transcriptional regulation. *Nat. Biotechnol.* **33**, 722–729 (2015).
46. Alkallas, R., Fish, L., Goodarzi, H. & Najafabadi, H. S. Inference of RNA decay rate from transcriptional profiling highlights the regulatory programs of Alzheimer's disease. *Nat. Commun.* **8**, 909 (2017).
47. Luo, Y., Na, Z. & Slavoff, S. A. P-Bodies: composition, properties, and functions. *Biochemistry* **57**, 2424–2431 (2018).
48. Standart, N. & Weil, D. P-Bodies: Cytosolic droplets for coordinated mRNA storage. *Trends Genet.* **34**, 612–626 (2018).
49. Tian, S., Curnutte, H. A. & Trcek, T. RNA granules: a view from the RNA perspective. *Molecules* **25**, 3130 (2020).
50. Kauer, M. et al. A molecular function map of Ewing's sarcoma. *PLoS ONE* **4**, e5415 (2009).
51. Orth, M. F. et al. Systematic multi-omics cell line profiling uncovers principles of Ewing sarcoma fusion oncogene-mediated gene regulation. *Cell Rep.* **41**, 111761 (2022).
52. Schoenberg, D. R. & Maquat, L. E. Regulation of cytoplasmic mRNA decay. *Nat. Rev. Genet* **13**, 246–259 (2012).
53. Houseley, J. & Tollervey, D. The many pathways of RNA degradation. *Cell* **136**, 763–776 (2009).
54. Youn, J.-Y. et al. Properties of stress granule and P-body proteomes. *Mol. Cell* **76**, 286–294 (2019).
55. Barreau, C., Watrin, T., Beverley Osborne, H. & Paillard, L. Protein expression is increased by a class III AU-rich element and tethered CUG-BP1. *Biochem. Biophys. Res. Commun.* **347**, 723–730 (2006).
56. Yan, Y.-B. Deadenylation: enzymes, regulation, and functional implications. *Wiley Interdiscip. Rev. RNA* **5**, 421–443 (2014).
57. Chen, C.-Y. A. & Shyu, A.-B. Mechanisms of deadenylation-dependent decay. *Wiley Interdiscip. Rev. RNA* **2**, 167–183 (2011).
58. Passmore, L. A. & Coller, J. Roles of mRNA poly(A) tails in regulation of eukaryotic gene expression. *Nat. Rev. Mol. Cell Biol.* **23**, 93–106 (2022).
59. Cassonnet, P. et al. Benchmarking a luciferase complementation assay for detecting protein complexes. *Nat. Methods* **8**, 990–992 (2011).
60. Boland, A. et al. Structure and assembly of the NOT module of the human CCR4-NOT complex. *Nat. Struct. Mol. Biol.* **20**, 1289–1297 (2013).
61. Lau, N. C. et al. Human Ccr4-Not complexes contain variable deadenylase subunits. *Biochem. J.* **422**, 443–453 (2009).
62. Boone, M. A. et al. The FLI portion of EWS/FLI contributes a transcriptional regulatory function that is distinct and separable from its DNA-binding function in Ewing sarcoma. *Oncogene* **40**, 4759–4769 (2021).
63. Ng, K. P. et al. Multiple aromatic side chains within a disordered structure are critical for transcription and transforming activity of EWS family oncoproteins. *Proc. Natl. Acad. Sci. USA* **104**, 479–484 (2007).
64. Lee, K. A. W. Molecular recognition by the EWS transcriptional activation domain. *Adv. Exp. Med. Biol.* **725**, 106–125 (2012).
65. Surdez, D. et al. STAG2 mutations alter CTCF-anchored loop extrusion, reduce cis-regulatory interactions and EWSR1-FLI1 activity in Ewing sarcoma. *Cancer Cell* **39**, 810–826.e9 (2021).
66. May, W. A. et al. Ewing sarcoma 11;22 translocation produces a chimeric transcription factor that requires the DNA-binding domain encoded by FLI1 for transformation. *Proc. Natl. Acad. Sci. USA* **90**, 5752–5756 (1993).
67. Welford, S. M., Hebert, S. P., Deneen, B., Arvand, A. & Denny, C. T. DNA binding domain-independent pathways are involved in EWS/FLI1-mediated oncogenesis. *J. Biol. Chem.* **276**, 41977–41984 (2001).
68. Boulay, G. et al. Cancer-specific retargeting of BAF complexes by a prion-like domain. *Cell* **171**, 163–178.e19 (2017).
69. Kato, M. et al. Cell-free formation of RNA granules: low complexity sequence domains form dynamic fibers within hydrogels. *Cell* **149**, 753–767 (2012).
70. Presman, D. M. et al. DNA binding triggers tetramerization of the glucocorticoid receptor in live cells. *Proc. Natl. Acad. Sci. USA* **113**, 8236–8241 (2016).
71. Digman, M. A., Dalal, R., Horwitz, A. F. & Gratton, E. Mapping the number of molecules and brightness in the laser scanning microscope. *Biophys. J.* **94**, 2320–2332 (2008).
72. Saulnier, O. et al. ERG transcription factors have a splicing regulatory function involving RBFOX2 that is altered in the EWS-FLI1 oncogenic fusion. *Nucleic Acids Res.* **49**, 5038–5056 (2021).
73. Knoop, L. L. & Baker, S. J. EWS/FLI alters 5′-splice site selection. *J. Biol. Chem.* **276**, 22317–22322 (2001).

74. Selvanathan, S. P. et al. Oncogenic fusion protein EWS-FLI1 is a network hub that regulates alternative splicing. *Proc. Natl. Acad. Sci. USA* **112**, E1307–E1316 (2015).
75. Selvanathan, S. P. et al. EWS-FLI1 modulated alternative splicing of ARID1A reveals novel oncogenic function through the BAF complex. *Nucleic Acids Res.* **47**, 9619–9636 (2019).
76. Sun, S., Zhang, Z., Fregoso, O. & Krainer, A. R. Mechanisms of activation and repression by the alternative splicing factors RBFOX1/2. *RNA* **18**, 274–283 (2012).
77. Mayya, V. K. & Duchaine, T. F. Ciphers and executioners: how 3′-untranslated regions determine the fate of messenger RNAs. *Front Genet* **10**, 6 (2019).
78. Barreau, C., Paillard, L. & Osborne, H. B. AU-rich elements and associated factors: are there unifying principles?. *Nucleic Acids Res.* **33**, 7138–7150 (2005).
79. Mukherjee, N. et al. Integrative regulatory mapping indicates that the RNA-binding protein HuR couples pre-mRNA processing and mRNA stability. *Mol. Cell* **43**, 327–339 (2011).
80. D'Agostino, V. G. et al. Dihydrotanshinone-I interferes with the RNA-binding activity of HuR affecting its post-transcriptional function. *Sci. Rep.* **5**, 1–15 (2015).
81. Lal, P. et al. Regulation of HuR structure and function by dihydrotanshinone-I. *Nucleic Acids Res.* **45**, 9514–9527 (2017).
82. Abdelmohsen, K. & Gorospe, M. Posttranscriptional regulation of cancer traits by HuR. *Wiley Interdiscip Rev RNA*. **1**, 214–229 (2010).
83. Wu, X. et al. Identification and Validation of Novel Small Molecule Disruptors of HuR-mRNA Interaction. *ACS Chem. Biol.* **10**, 1476–1484 (2015).
84. Lawlor, E. R., Scheel, C., Irving, J. & Sorensen, P. H. B. Anchorage-independent multi-cellular spheroids as an in vitro model of growth signaling in Ewing tumors. *Oncogene* **21**, 307–318 (2002).
85. Volchenboum, S. L. et al. Gene expression profiling of ewing sarcoma tumors reveals the prognostic importance of tumor-stromal interactions: a report from the children's oncology group. *J. Pathol. Clin. Res.* **1**, 83–94 (2015).
86. Scotlandi, K. et al. Overcoming resistance to conventional drugs in Ewing sarcoma and identification of molecular predictors of outcome. *J. Clin. Oncol.* **27**, 2209–2216 (2009).
87. Savola, S. et al. High expression of complement component 5 (C5) at tumor site associates with superior survival in Ewing's sarcoma family of tumour patients. *ISRN Oncol.* **2011**, 168712 (2011).
88. Postel-Vinay, S. et al. Common variants near TARDBP and EGR2 are associated with susceptibility to Ewing sarcoma. *Nat. Genet* **44**, 323–327 (2012).
89. Vanharanta, S. et al. Loss of the multifunctional RNA-binding protein RBM47 as a source of selectable metastatic traits in breast cancer. *Elife* **3**, e02734 (2014).
90. Griseri, P. & Pagès, G. Regulation of the mRNA half-life in breast cancer. *World J. Clin. Oncol.* **5**, 323–334 (2014).
91. Choder, M. mRNA imprinting: additional level in the regulation of gene expression. *Cell Logist.* **1**, 37–40 (2011).
92. Boija, A. et al. Transcription factors activate genes through the phase-separation capacity of their activation domains. *Cell* **175**, 1842–1855.e16 (2018).
93. Hnisz, D., Shrinivas, K., Young, R. A., Chakraborty, A. K. & Sharp, P. A. A phase separation model for transcriptional control. *Cell* **169**, 13–23 (2017).
94. Chong, S. et al. Imaging dynamic and selective low-complexity domain interactions that control gene transcription. *Science* **361**, eaar2555 (2018).
95. Banani, S. F. et al. Compositional Control of Phase-Separated. *Cell. Bodies. Cell* **166**, 651–663 (2016).
96. Chong, S. et al. Tuning levels of low-complexity domain interactions to modulate endogenous oncogenic transcription. *Mol. Cell* **82**, 2084–2097.e5 (2022).
97. Mitrea, D. M., Mittasch, M., Gomes, B. F., Klein, I. A. & Murcko, M. A. Modulating biomolecular condensates: a novel approach to drug discovery. *Nat. Rev. Drug Discov.* **21**, 841–862 (2022).
98. Biesaga, M., Frigolé-Vivas, M. & Salvatella, X. Intrinsically disordered proteins and biomolecular condensates as drug targets. *Curr. Opin. Chem. Biol.* **62**, 90–100 (2021).
99. Basu, S. et al. Rational optimization of a transcription factor activation domain inhibitor. *Nat. Struct. Mol. Biol.* **30**, 1958–1969 (2023).
100. Arvand, A., Welford, S. M., Teitell, M. A. & Denny, C. T. The COOH-terminal domain of FLI-1 is necessary for full tumorigenesis and transcriptional modulation by EWS/FLI-1. *Cancer Res* **61**, 5311–5317 (2001).
101. Wang, J. et al. Multiple functions of the RNA-binding protein HuR in cancer progression, treatment responses and prognosis. *Int J. Mol. Sci.* **14**, 10015–10041 (2013).
102. Marchetto, A. et al. Oncogenic hijacking of a developmental transcription factor evokes vulnerability toward oxidative stress in Ewing sarcoma. *Nat. Commun.* **11**, 2423 (2020).
103. Su, X. A. et al. RAD21 is a driver of chromosome 8 gain in Ewing sarcoma to mitigate replication stress. *Genes Dev.* **35**, 556–572 (2021).
104. Weaver, D. T. et al. Network potential identifies therapeutic miRNA cocktails in Ewing sarcoma. *PLoS Comput Biol.* **17**, e1008755 (2021).
105. Yue, J. et al. The multifaceted mechanisms of Dihydrotanshinone I in the treatment of tumors. *Biomed. Pharmacother.* **175**, 116635 (2024).
106. Atanassov, I. I., Atanassov, I. I., Etchells, J. P. & Turner, S. R. A simple, flexible and efficient PCR-fusion/Gateway cloning procedure for gene fusion, site-directed mutagenesis, short sequence insertion and domain deletions and swaps. *Plant Methods* **5**, 14 (2009).
107. Lykke-Andersen, J., Shu, M. D. & Steitz, J. A. Human Upf proteins target an mRNA for nonsense-mediated decay when bound downstream of a termination codon. *Cell* **103**, 1121–1131 (2000).
108. Twyffels, L. et al. A masked PY-NLS in Drosophila TIS11 and its mammalian homolog tristetraprolin. *PLoS ONE* **8**, e71686 (2013).
109. Dobin, A. et al. STAR: ultrafast universal RNA-seq aligner. *Bioinformatics* **29**, 15–21 (2013).
110. Anders, S., Pyl, P. T. & Huber, W. HTSeq-a Python framework to work with high-throughput sequencing data. *Bioinformatics* **31**, 166–169 (2015).
111. Love, M. I., Huber, W. & Anders, S. Moderated estimation of fold change and dispersion for RNA-seq data with DESeq2. *Genome Biol.* **15**, 550 (2014).
112. Kim, D., Paggi, J. M., Park, C., Bennett, C. & Salzberg, S. L. Graph-based genome alignment and genotyping with HISAT2 and HISAT-genotype. *Nat. Biotechnol.* **37**, 907–915 (2019).
113. McLeay, R. C. & Bailey, T. L. Motif Enrichment Analysis: a unified framework and an evaluation on ChIP data. *BMC Bioinforma.* **11**, 165 (2010).
114. Mészáros, B., Erdos, G. & Dosztányi, Z. IUPred2A: context-dependent prediction of protein disorder as a function of redox state and protein binding. *Nucleic Acids Res.* **46**, W329–W337 (2018).
115. Obradovic, Z. et al. Predicting intrinsic disorder from amino acid sequence. *Proteins* **53**, 566–572 (2003).
116. Yang, Z. R., Thomson, R., McNeil, P. & Esnouf, R. M. RONN: the bio-basis function neural network technique applied to the detection of natively disordered regions in proteins. *Bioinformatics* **21**, 3369–3376 (2005).
117. Hanson, J., Yang, Y., Paliwal, K. & Zhou, Y. Improving protein disorder prediction by deep bidirectional long short-term memory recurrent neural networks. *Bioinformatics* **33**, 685–692 (2017).

118. Wang, S., Ma, J. & Xu, J. AUCpreD: proteome-level protein disorder prediction by AUC-maximized deep convolutional neural fields. *Bioinformatics* **32**, i672–i679 (2016).
119. Walsh, I., Martin, A. J. M., Di Domenico, T. & Tosatto, S. C. E. ESpritz: accurate and fast prediction of protein disorder. *Bioinformatics* **28**, 503–509 (2012).
120. Kozlowski, L. P. & Bujnicki, J. M. MetaDisorder: a meta-server for the prediction of intrinsic disorder in proteins. *BMC Bioinforma.* **13**, 111 (2012).
121. Hirose, S., Shimizu, K., Kanai, S., Kuroda, Y. & Noguchi, T. POODLE-L: a two-level SVM prediction system for reliably predicting long disordered regions. *Bioinformatics* **23**, 2046–2053 (2007).
122. Jumper, J. et al. Highly accurate protein structure prediction with AlphaFold. *Nature* **596**, 583–589 (2021).
123. Varadi, M. et al. AlphaFold protein structure database: massively expanding the structural coverage of protein-sequence space with high-accuracy models. *Nucleic Acids Res.* **50**, D439–D444 (2022).
124. Pabis, M. et al. HuR biological function involves RRM3-mediated dimerization and RNA binding by all three RRMs. *Nucleic Acids Res.* **47**, 1011–1029 (2019).
125. de Vries, S. J., van Dijk, M. & Bonvin, A. M. J. J. The HADDOCK web server for data-driven biomolecular docking. *Nat. Protoc.* **5**, 883–897 (2010).
126. Berendsen, H. J. C., van der Spoel, D. & van Drunen, R. GROMACS: A message-passing parallel molecular dynamics implementation. *Comput Phys. Commun.* **91**, 43–56 (1995).
127. Abraham, M. J. et al. GROMACS: High performance molecular simulations through multi-level parallelism from laptops to supercomputers. *SoftwareX* **1–2**, 19–25 (2015).
128. Best, R. B. et al. Optimization of the additive CHARMM all-atom protein force field targeting improved sampling of the backbone φ, ψ and side-chain χ(1) and χ(2) dihedral angles. *J. Chem. Theory Comput* **8**, 3257–3273 (2012).
129. Humphrey, W., Dalke, A. & Schulten, K. VMD: visual molecular dynamics. *J. Mol. Graph* **14**, 33–38 (1996).
130. Baldauf, M. C. et al. Robust diagnosis of Ewing sarcoma by immunohistochemical detection of super-enhancer-driven EWSR1-ETS targets. *Oncotarget* **9**, 1587–1601 (2018).
131. Stein, C. K. et al. Removing batch effects from purified plasma cell gene expression microarrays with modified ComBat. *BMC Bioinforma.* **16**, 63 (2015).
132. Ebegboni, V. J. et al. ETS1, a Target gene of the EWSR1::FLI1 fusion oncoprotein, regulates the expression of the focal adhesion protein TENSIN3. *Mol. Cancer Res.* **22**, 625–641 (2024).
133. Buchou, C. et al. Upregulation of the mevalonate pathway through EWSR1-FLI1/EGR2 regulatory axis confers ewing cells exquisite sensitivity to statins. *Cancers* **14**, 2327 (2022).
134. Lindén, M. et al. FET family fusion oncoproteins target the SWI/SNF chromatin remodeling complex. *EMBO Rep.* **20**, e45766 (2019).

Acknowledgements

We thank Dr. O. Delattre for kindly sharing the shA673-1c and shSK-E17T cell lines. We thank Dr. Y. Beguin for kindly providing hMSCs. We thank the GIGA-Viral Vectors, Imaging and Genomics facilities (University of Liege) for technical support and helpful assistance. We thank S. Draga (University of Bucharest) for helpful assistance with docking and molecular dynamics analyses. Computational resources have been provided by the Consortium des Équipements de Calcul Intensif (CÉCI), funded by the Belgian National Fund for Scientific Research (F.R.S.-FNRS) and by the Walloon Region. This study was supported by the University of Liège (ULiège), the Belgian National Fund for Scientific Research (F.R.S-FNRS), Télévie, Fondation contre le Cancer and the Fondation Léon Fredericq. The laboratory of T.G.P.G. is supported by grants from the European Research Council (ERC CoG 2023 #101122595), the Ministry of Education and Research (BMBF; SMART-CARE and HEROES-AYA), and the Barbara and Wilfried Mohr foundation. F.H.G was supported by scholarships of the German Cancer Aid and the German Academic Scholarship Foundation.

Author contributions

F.D. and B.G. designed the study and wrote the manuscript. B.G., L.O., J.B., G.F., E.L., E.M., Z.E.O.H., J.D., E.H., M.C. and L.D. performed the experiments. B.G., A.L., T.M.OG. and L.O. conducted bioinformatic analyses. F.C-A. and F.H.G. conducted and A.B. and R.I. participated to the in vivo experiments. F.C-A. carried out the survival analysis. F.D., K.A.W.L., V.K., C.G., T.G.P.G., A.B., L.M., A.K.J., R.I. and J-C.T. provided necessary reagents, data, and conceptual advice.

Competing interests

The authors declare no competing interests.

Additional information

Supplementary information The online version contains supplementary material available at https://doi.org/10.1038/s41467-025-61725-x.

Correspondence and requests for materials should be addressed to Franck Dequiedt.

Peer review information *Nature Communications* thanks Gagan Gupta and the other anonymous reviewer(s) for their contribution to the peer review of this work. A peer review file is available.

[1]Laboratory of Gene Expression and Cancer, GIGA Institute, University of Liège (ULiège), Liège, Belgium. [2]Division of Oncology and Children's Research Centre, University Children's Hospital Zurich, Zurich, Switzerland. [3]Laboratory of Receptor Biology and Gene Expression, National Cancer Institute, National Institutes of Health, Bethesda, USA. [4]Genomics Platform, GIGA Institute, University of Liège (ULiège), Liège, Belgium. [5]Department of Pathology & Laboratory

Medicine, Tulane University School of Medicine, New Orleans, USA. [6]Department of Integrative Structural and Computational Biology, The Herbert Wertheim UF Scripps Institute for Biomedical Innovation & Technology, Jupiter, USA. [7]Division of Life Science, The Hong Kong University of Sci. & Tech, Clear Water Bay, Kowloon, Hong Kong SAR, China. [8]Laboratory of Molecular Biology of the Gene, Department of Molecular Biology, Free University of Brussels (ULB), 6041 Gosselies, Belgium. [9]Université Franche-Comté, INSERM, EFS BFC, UMR1098, « Interactions Hôte-Greffon-Tumeur/Ingénierie Cellulaire et Génique », F-25000 Besançon, France. [10]EPIGENExp platform, Université Franche-Comté, F-25000 Besançon, France. [11]Hopp Children's Cancer Center Heidelberg (KiTZ), Heidelberg, Germany. [12]National Center for Tumor Diseases (NCT), NCT Heidelberg, a partnership between DKFZ and Heidelberg University Hospital, Heidelberg, Germany. [13]Division of Translational Pediatric Sarcoma Research, German Cancer Research Center (DKFZ), German Cancer Consortium (DKTK), Heidelberg, Germany. [14]Soft-Tissue Sarcoma research group (B380), German Cancer Research Center (DKFZ), Heidelberg, Germany. [15]Department of pediatric Oncology, Hematology and Immunology, Heidelberg University Hospital, Heidelberg, Germany. [16]Research Group Proteomics and Cancer Cell Signaling, Hopp Children's Cancer Center Heidelberg (KiTZ), Heidelberg, Germany. [17]Institute of Pathology, Heidelberg University Hospital, Heidelberg, Germany. [18]Laboratory of Viral Interactomes Networks, GIGA Institute, University of Liège (ULiège), 4000 Liège, Belgium. ✉e-mail: fdequiedt@uliege.be